J. Fluid Mech. (1992), *vol.* 236, *pp.* 281–318
Printed in Great Britain

Kinematic simulation of homogeneous turbulence by unsteady random Fourier modes

By J. C. H. FUNG, J. C. R. HUNT, N. A. MALIK AND R. J. PERKINS

Department of Applied Mathematics and Theoretical Physics, University of Cambridge, Silver Street, Cambridge CB3 9EW, UK

(Received 5 June 1990 and in revised form 26 August 1991)

The velocity field of homogeneous isotropic turbulence is simulated by a large number (38–1200) of random Fourier modes varying in space and time over a large number (>100) of realizations. They are chosen so that the flow field has certain properties, namely (i) it satisfies continuity, (ii) the two-point Eulerian spatial spectra have a known form (e.g. the Kolmogorov inertial subrange), (iii) the time dependence is modelled by dividing the turbulence into large- and small-scales eddies, and by assuming that the large eddies advect the small eddies which also decorrelate as they are advected, (iv) the amplitudes of the large- and small-scale Fourier modes are each statistically independent and each Gaussian. The structure of the velocity field is found to be similar to that computed by direct numerical simulation with the same spectrum, although this simulation underestimates the lengths of tubes of intense vorticity.

Some new results and concepts have been obtained using this kinematic simulation: (*a*) for the inertial subrange (which cannot yet be simulated by other means) the simulation confirms the form of the Eulerian frequency spectrum $\phi_{11}^{\mathrm{E}} = C^{\mathrm{E}} \epsilon^{\frac{2}{3}} U_0^2 \omega^{-\frac{5}{3}}$, where ϵ, U_0, ω are the rate of energy dissipation per unit mass, large-scale r.m.s. velocity, and frequency. For isotropic Gaussian large-scale turbulence at very high Reynolds number, $C^{\mathrm{E}} \approx 0.78$, which is close to the computed value of 0.82; (*b*) for an observer moving with the large eddies the 'Eulerian–Lagrangian' spectrum is $\phi_{11}^{\mathrm{EL}} = C^{\mathrm{EL}} \epsilon \omega^{-2}$, where $C^{\mathrm{EL}} \approx 0.73$; (*c*) for an observer moving with a fluid particle the Lagrangian spectrum $\phi_{11}^{\mathrm{L}} = C^{\mathrm{L}} \epsilon \omega^{-2}$, where $C^{\mathrm{L}} \approx 0.8$, a value consistent with the atmospheric turbulence measurements by Hanna (1981) and approximately equal to C^{EL}; (*d*) the mean-square relative displacement of a pair of particles $\langle \Delta^2 \rangle$ tends to the Richardson (1926) and Obukhov (1941) form $\langle \Delta^2 \rangle = G_\Delta \epsilon t^3$, provided that the subrange extends over four decades in energy, and a suitable origin is chosen for the time t. The constant G_Δ is computed and is equal to 0.1 (which is close to Tatarski's 1960 estimate of 0.06); (*e*) difference statistics (i.e. displacement from the initial trajectory) of *single* particles are also calculated. The exact result that $\langle Y^2 \rangle = G_Y \epsilon t^3$ with $G_Y = 2\pi C^{\mathrm{L}}$ is approximately confirmed (although it requires an even larger inertial subrange than that for $\langle \Delta^2 \rangle$). It is found that the ratio $\mathscr{R}_G = 2\langle Y^2 \rangle / \langle \Delta^2 \rangle \approx 100$, whereas in previous estimates $\mathscr{R}_G \approx 1$, because for much of the time pairs of particles move together around vortical regions and only separate for the proportion of the time (of $O(f_c)$) they spend in straining regions where streamlines diverge. It is estimated that $\mathscr{R}_G \approx O(f_c^{-3})$. Thus relative diffusion is both a 'structural' (or 'topological') process as well as an intermittent inverse cascade process determined by increasing eddy scales as the particles separate; (*f*) statistics of large-scale turbulence are also computed, including the

Lagrangian timescale, the pressure spectra and correlations, and these agree with predictions of Batchelor (1951), Hinze (1975) and George *et al.* (1984).

1. Introduction

In many fields of turbulence research, it is as necessary to be able to compute or model actual flow fields as they evolve as it is to know the statistics of the turbulence (e.g. spectra, correlations etc). This is because many processes involving turbulence are not well enough understood to be quantified in terms of the statistics. For example the effect of turbulence on chemical reactions (e.g. Broadwell & Breidenthal 1982) or on particle trajectories (e.g. Maxey 1987) or on bubble concentrations (e.g. Hunt *et al.* 1988) can best be understood and modelled in terms of actual flow structures. One reason for this is that certain reactions or bubble concentrations tends to be located in vortical regions of the flow, whilst particles appear to move in regions between vortices. These highly non-uniform processes and distributions cannot be modelled satisfactorily in terms of the statistics of the velocity field. Instead it is necessary to compute reacting species or the motion of bubbles and particles as they are transported in the actual flow.

When such studies have progressed further it is likely that reliable models will emerge relating these complex processes to the statistics of the turbulence. For example several research groups are exploring the use of stochastic models for the fluctuating velocity at the site of a particle moving randomly through turbulent flows (e.g. random flight models). The essential feature of these models is that they assume certain relations between Eulerian and Lagrangian statistics which can only be tested in detail using a computation of a velocity field. In studies of combustion and mixing, models are being developed based on the large scale deterministic flow structure within the turbulence (e.g. Broadwell & Breidenthal 1982; Peters & Williams 1988). There are also smaller scale processes, such as the coagulation of small particles or the break-up of bubbles and transmission of waves through turbulence, where the small-scale velocity field must be simulated.

These are practical reasons for developing methods for computational modelling of actual flow fields. But the study of the fundamental dynamics and kinematics of turbulence also requires simulations of actual flow fields. Certain important concepts of turbulence can be explored even with simulations that are not quite accurate, partly because these concepts are based on dimensional scaling arguments which are equally applicable to a sum of Fourier modes as to a nonlinear flow field. For example we can explore how the distance $\langle \Delta \rangle$ between pairs of fluid elements increases in different flow fields (or when the inertial range law $\langle \Delta^2 \rangle \propto t^3$ is valid), the relationship between Lagrangian and Eulerian statistics, and how they depend on the assumptions about the dependence on time of the Fourier modes in the simulation. By comparing this simulation with those derived from computations of the full nonlinear equations, we learn from their similarity that many of the broad features of the flow field are insensitive to the dynamics (as was suggested in earlier studies on turbulence, e.g. Batchelor 1953, pp. 6–7). The specific dynamics of the Euler equation control the statistics, but may only affect local details of the velocity field (e.g. the length of tubes of intense vorticity).

Most simulations of turbulent flow fields use exact or approximate solutions to the equations of motion which are continuously solved to represent the evolving flow field. In a direct numerical simulation of turbulence the flow is calculated from first

principles without any closure assumptions. All that is needed are proper initial and boundary conditions, an accurate and efficient numerical solution scheme and a large computer (Rogallo & Moin 1984). Although some progress has been made in the efficiency and accuracy of computational algorithms, particularly in the adaptation of spectral methods, the primary limitation on our ability to simulate high-Reynolds-number turbulence is the speed and memory size of the computing hardware. Though a turbulent Reynolds number of 150 has been achieved (Vincent & Meneguzzi 1991), this is still too low for the study of many turbulence phenomena found in geophysical flows. This restriction on Reynolds number is avoided by computing solutions to the dynamical equations only for the large scales, and modelling the small scales in terms of a local eddy viscosity acing on the large scales. This is the method of large-eddy simulation.

In this paper random flow fields are generated from certain statistical distributions that are known from measurements or direct simulations, but the flow fields do not necessarily satisfy the dynamical equations nor do they have all the known statistical distributions. We extend the methods of Kraichnan (1970) and Drummond, Duane & Horgan (1984), who studied turbulent diffusion using statistically independent random Fourier modes, but not a full spectrum. No attempt was made by these authors to model the details of the inertial range. However, some important concepts emerged from those studies about the Lagrangian timescale and the role of molecular processes in turbulent diffusion.

The essential objective here is to use the specified velocity field to predict some new results, which can be compared with experiments (or other kinds of simulation). If the simulation is at all useful it should also lead to some new concepts. The construction and use of kinematic simulations (KS) ought to be based on the results obtained from dynamical simulations and from experiments. One can also regard this simulation as a convenient way of providing an accessible repository or reference for much of our present knowledge of two-point/two-time Eulerian/Lagrangian statistics. It may enable investigators using turbulent flow fields to estimate many widely different kinds of statistics that are needed for different applications. (Brief accounts of this simulation and its applications have been reported by Fung *et al.* 1991, Hunt *et al.* 1991.)

The kinematic simulation of homogeneous turbulence presented here is not grid-based, and does not require the solution of any set of equations, so it can be easily programmed on any computer. It takes a long time to run on a small computer; it is more convenient to use a large one! It is ideally suited to parallel computations. The method can be extended to allow for shear (Carruthers *et al.* 1990) and for the effects of rigid walls or distortion of turbulence at a density interface (Perkins *et al.* 1990), following the approaches of Lee, Kim & Moin (1990) and Turfus & Hunt (1987).

2. Method

For homogeneous turbulent flow defined within a space $|x_i| < X_i$ that is stationary in time (within a period T), the velocity field can be represented as a Fourier series in the limits $N, P_\omega \to \infty$:

$$\boldsymbol{u}(\boldsymbol{x},t) = \sum_{n_i=-N_k}^{N_k} \sum_{p=-P_\omega}^{P_\omega} \boldsymbol{S}_{n_i p} \exp\{\mathrm{i}(k_{n_i} x_i + \omega_p t)\} \quad (i = 1,2,3), \tag{2.1}$$

where $k_{n_i} = 2\pi n_i / X_i$, $\omega_p = 2\pi p / T$ and $\boldsymbol{S}_{n_i p}$ are random vector Fourier coefficients.

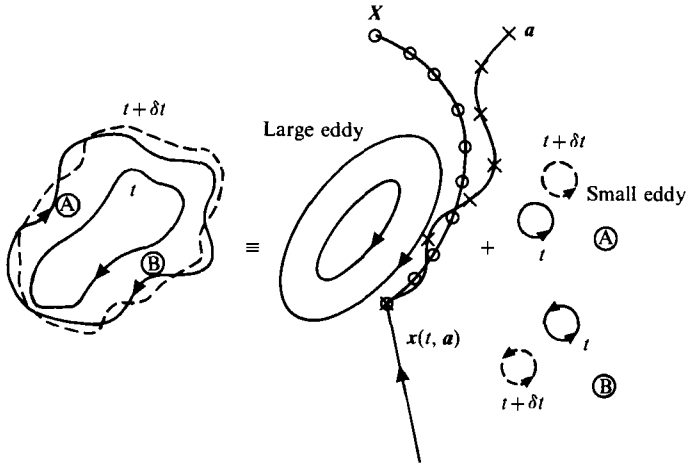

FIGURE 1. Flow field composed of large-scale eddies and small-scale eddies that are transported by the large scales. ——, Streamlines; + + + +, fluid particle trajectories, $\boldsymbol{x}(t,\boldsymbol{a}) = \int_0^t (\boldsymbol{u}_l + \boldsymbol{u}_s)\,\mathrm{d}t'$; ○ ○ ○ ○, trajectory of a small-scale eddy advected from $\boldsymbol{X}(t=0)$ to position $\boldsymbol{x}(t)$ at time t (see $\boldsymbol{X}$ in (2.8)), i.e. $\int_0^t \boldsymbol{u}_l(\boldsymbol{x}_l(t'),t')\,\mathrm{d}t'$.

For finite values of N_k, P_ω, (2.1) is an approximation, the accuracy of which depends on the form of the velocity field. If there is a mean flow, we take coordinates moving with the mean flow.

The wavenumbers distributed here in a Cartesian frame can also be distributed within a spherical coordinate system over N_k shells (where $|\boldsymbol{\kappa}| = k =$ constant) and M_θ angles. So the nth spatial mode in (2.1) becomes an mnth mode. It is found that a satisfactory representation is obtained by including only a limited number of temporal (frequency) modes for each spatial (wavenumber) mode, so that ω_p is a function of $|\boldsymbol{\kappa}_n|$. Therefore ω_p is written as ω_{np}. Also, to ensure that the velocity field is solenoidal ($\nabla\cdot\boldsymbol{u} = 0$), the vector Fourier coefficient is rewritten as $\boldsymbol{S}_{n_i p} = \hat{\boldsymbol{S}}_{mnp} \wedge \boldsymbol{\kappa}_{mn}$ where $\hat{\boldsymbol{S}}_{mnp} = \frac{1}{2}(\boldsymbol{a}_{mnp} \pm \mathrm{i}\boldsymbol{b}_{mnp})$ for all n. Here $\boldsymbol{a}_{mnp}$ and $\boldsymbol{b}_{mnp}$ are real, random vectors uniformly distributed over all directions and statistically independent, in the sense that

$$\langle \boldsymbol{a}_{m_1 n_1 p_1} \boldsymbol{a}_{m_2 n_2 p_2} \rangle = 0 \quad \text{if} \quad m_1 \neq m_2, n_1 \neq n_2 \text{ or } p_1 \neq p_2$$

because the flow is homogeneous and isotropic.

2.1. *The velocity field*

Hence, following Kraichnan (1970) and Drummond *et al.* (1984), (2.1) is written as

$$\boldsymbol{u}(\boldsymbol{x},t) = \sum_{m=1}^{M_\theta} \sum_{n=1}^{n=N_k} \sum_{p=1}^{P_\omega} [(\boldsymbol{a}_{mnp} \wedge \hat{\boldsymbol{\kappa}}_{mn}) \cos\{\boldsymbol{\kappa}_{mn}\cdot\boldsymbol{x} + \omega_{np} t\} + (\boldsymbol{b}_{mnp} \wedge \hat{\boldsymbol{\kappa}}_{mn}) \sin\{\boldsymbol{\kappa}_{mn}\cdot\boldsymbol{x} + \omega_{np} t\}], \quad (2.2)$$

where $\hat{\boldsymbol{\kappa}}_{mn} = \boldsymbol{\kappa}_{mn}/k_n$ and $k_n = |\boldsymbol{\kappa}_{mn}|$ for all m.

The statistical distribution of $\boldsymbol{a}_{mnp}$, $\boldsymbol{b}_{mnp}$ and the distribution of $\boldsymbol{\kappa}_{mn}$ are defined in §2.5.

The time dependence of turbulence is actually determined by the nonlinear dynamical interactions between different modes (e.g. vortex stretching) and by the kinematic process of non-uniform unsteady advection of the vorticity field by the velocity field, which implies large-scale eddies advecting small-scale eddies (figure 1).

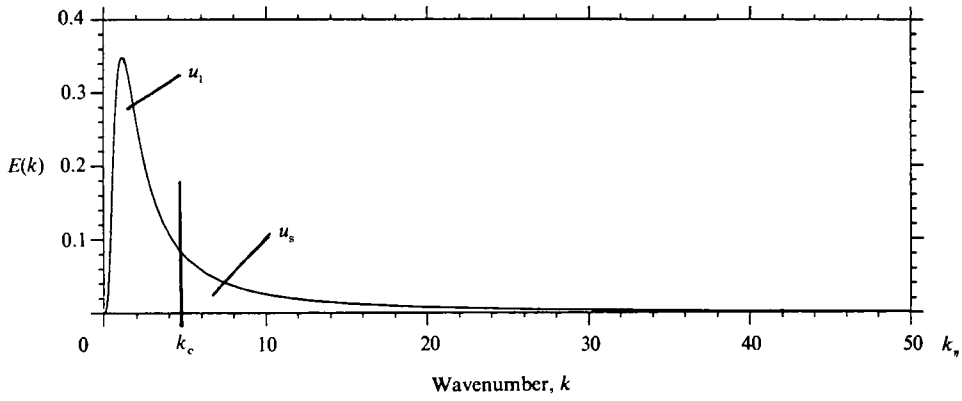

FIGURE 2. Splitting the von Kármán energy spectrum into large and small scales. $E(k) \to k^4$ as $k \to 0$ and $E(k) \to k^{-\frac{5}{3}}$ as $k \to \infty$.

The novel feature of our simulation is modelling these effects by choosing ω_{np} and $\boldsymbol{\kappa}_{mn}$ appropriately.

The temporal structure of the flow is determined by the frequency ω_{np} which we model in two different ways, and which we refer to here as the kinetic simulation sweeping model (henceforth KSSM) and the kinetic simulation inertial model (henceforth KSIM). In KSSM we divide the velocity field into large- and small-scale fields ($\boldsymbol{u}_l$ and $\boldsymbol{u}_s$) using a cut-off wavenumber k_c to divide the wavenumber range (figure 2). The velocity field is given by the sum of these two fields:

$$\boldsymbol{u}(\boldsymbol{x}, t) = \boldsymbol{u}_l(\boldsymbol{x}, t) + \boldsymbol{u}_s(\boldsymbol{x}, t). \tag{2.3}$$

The temporal fluctuations of the small-scale velocity field are partly caused by the non-uniform advection of the small scales by the large scales and partly by their dynamical interactions which lead to a decorrelation in this randomly moving frame of reference. In KSSM we model ω_{np} to account for both these processes.

In KSIM we focus on the relative motion of particle pairs at small separations, so the large-scale field can be neglected; in the small-scale field $\boldsymbol{u}_s(\boldsymbol{x}, t)$, we model ω_{np} by choosing a finite number of temporal modes for each wavenumber (figure 3). (As expected the statistics of the smallest scales derived by the two simulations are equivalent.)

Sweeping Model: KSSM

For KSSM we assume that the large eddies move randomly and independently of each other; this corresponds to a random shift in the relative phases of the large modes. Alternatively they might be computed by a large-eddy simulation. Also, in KSSM the time dependence is modelled in the simplest possible way by assuming a single frequency mode for each wavenumber mode. Therefore, we suppress the 'p' in all the terms in (2.2), i.e. $P_\omega = 1, \omega_{np} = \omega_n$. Also we take a single directional wavenumber on each shell in wavenumber space, so that $M_\theta = 1$. Then $\boldsymbol{a}_{mnp} \to \boldsymbol{a}_n$, $\boldsymbol{b}_{mnp} \to \boldsymbol{b}_n$. These random vectors $\boldsymbol{a}_n, \boldsymbol{b}_n$ and the wave vectors $\boldsymbol{\kappa}_n$ are defined in §2.5.

The large-scale motion $\boldsymbol{u}_l$ is modelled by $N_c - 1$ modes in which the time dependence is expressed as a random time-varying displacement of the spatial Fourier modes:

$$\boldsymbol{u}_l(\boldsymbol{x}, t) = \sum_{n=1}^{N_c-1} u_{l_n}(\boldsymbol{x}, t), \tag{2.4a}$$

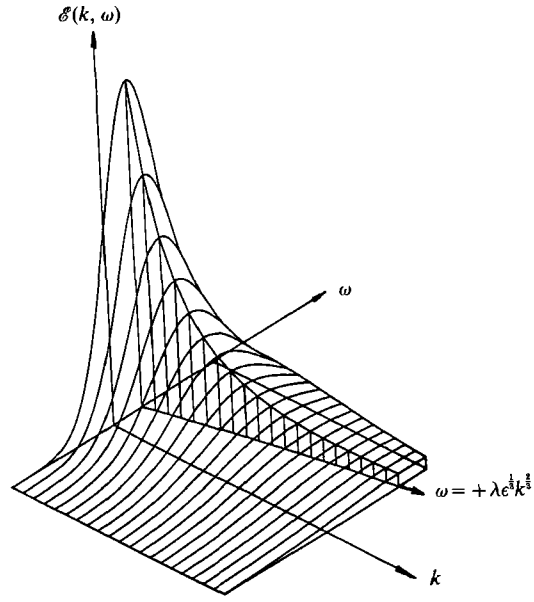

FIGURE 3. The probability distribution of ω. The peak in the distibution (for a given k) lies at $+\lambda\epsilon^{\frac{1}{3}}k^{\frac{2}{3}}$ and there is another (not shown) at $-\lambda\epsilon^{\frac{1}{3}}k^{\frac{2}{3}}$. For KSSM, ω is a δ-function, i.e. $P(\omega_n) = \delta(\omega_n \pm \lambda\epsilon^{\frac{1}{3}}k^{\frac{2}{3}})$; for KSIM, ω_{nm} is chosen from the probability distribution of $P(\omega)$.

where

$$\boldsymbol{u}_{1_n}(\boldsymbol{x},t) = (\boldsymbol{a}_n \wedge \hat{\boldsymbol{\kappa}}_n)\cos\{\boldsymbol{\kappa}_n\cdot(\boldsymbol{x}-\boldsymbol{\zeta}_n(\boldsymbol{\kappa}_n,t))\} + (\boldsymbol{b}_n \wedge \hat{\boldsymbol{\kappa}}_n)\sin\{\boldsymbol{\kappa}_n\cdot(\boldsymbol{x}-\boldsymbol{\zeta}_n(\boldsymbol{\kappa}_n,t))\}. \quad (2.4b)$$

Here $\omega_n = \boldsymbol{\kappa}_n\cdot\boldsymbol{\zeta}_n$, where $\boldsymbol{\zeta}_n(\boldsymbol{\kappa}_n,t)$ is a random displacement for the wavenumber $\boldsymbol{\kappa}_n$ which is induced by a random Gaussian advective velocity $\boldsymbol{W}_{k_n}(t)$. At time $t = 0$, $\boldsymbol{\zeta}_n(\boldsymbol{\kappa}_n,t) = 0$, thus

$$\boldsymbol{\zeta}_n(\boldsymbol{\kappa}_n,t) = \int_0^t \boldsymbol{W}_{k_n}(t')\,\mathrm{d}t'. \quad (2.5)$$

Since the eddies are advected by other eddies, it is assumed that $\boldsymbol{W}_{k_n}(t)$ is a random vector field with zero mean and variance equal to that of the nth mode of the velocity field, i.e. $\langle \boldsymbol{W}^2_{k_n}(t)\rangle = \langle u^2_{1_n}(\boldsymbol{x},t)\rangle$. Since the large scales of homogeneous isotropic turbulence are Gaussian and approximately Markovian, it is assumed that the modes $\boldsymbol{W}_{k_n}(t)$ of the advective velocity field have exponential correlation functions and timescales equal to the times taken by large eddies to pass each other, i.e. $T_n = 1/(\sigma_W k_n)$.

The spatial structure of the small-scale field $\boldsymbol{u}_s$ is modelled as in (2.4). The temporal variation of the small scales (for lengthscales greater than the Kolmogorov scale) is given in terms of $\boldsymbol{u}_1$ and $\boldsymbol{u}_s$ by the equation

$$\partial\boldsymbol{u}_s/\partial t = \underbrace{-\boldsymbol{u}_1\cdot\nabla\boldsymbol{u}_s}_{\text{advection}} \underbrace{-\,[(\boldsymbol{u}_s\cdot\nabla)\boldsymbol{u}_1 + (\boldsymbol{u}_1\cdot\nabla)\boldsymbol{u}_s + 1/\rho\,\nabla p]}_{\text{decorrelation}}. \quad (2.6)$$

The advection term which is the contribution of large scales advecting small scales can be modelled by considering the neglect of the 'decorrelation' terms. Thus the

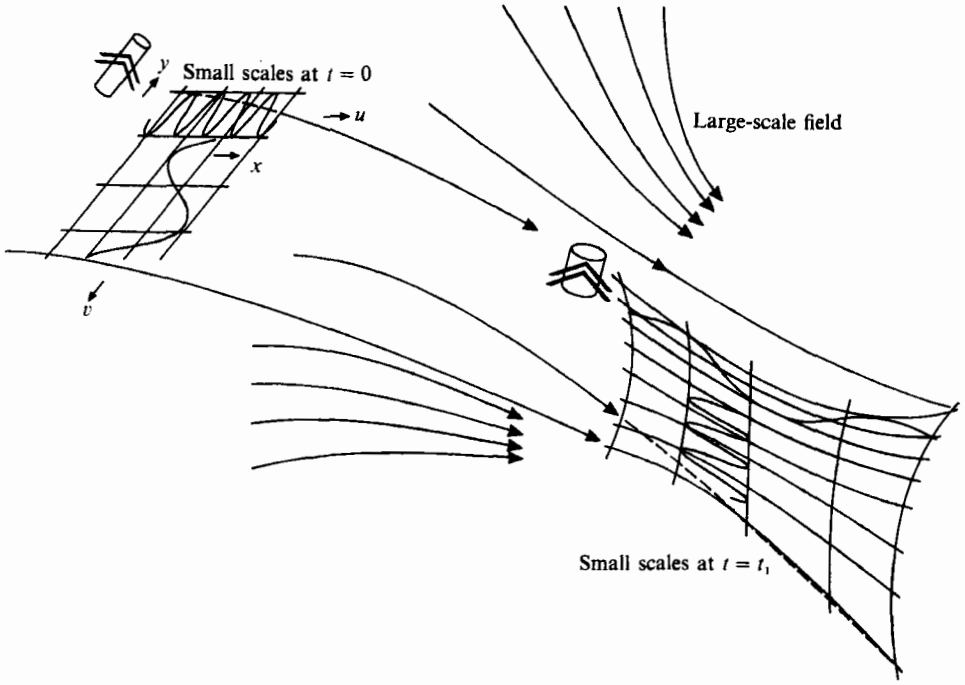

FIGURE 4. Diagram showing the distortion of the small-scale velocity field by the large-scale velocity field. The velocity components $u(x)$ and $v(y)$ due to a single wave mode change as the small field is displaced and deformed by the large field. But the change in vorticity is not explicitly simulated.

velocity at each point $\boldsymbol{x}$ would be equal to its value at an earlier time ($t = 0$) at the position $\boldsymbol{X}$ from where a material point was advected to $\boldsymbol{x}$ (figure 1). But as a material point is advected by the large scales, the velocity changes on a timescale $1/\omega_n'$. Thence

$$\boldsymbol{u}_s(\boldsymbol{x}, t) = \sum_{n=N_c}^{N_k} [(\boldsymbol{a}_n \wedge \hat{\boldsymbol{\kappa}}_n) \cos[\boldsymbol{\kappa}_n \cdot \boldsymbol{X} - \omega_n' t] + (\boldsymbol{b}_n \wedge \hat{\boldsymbol{\kappa}}_n) \sin[\boldsymbol{\kappa}_n \cdot \boldsymbol{X} - \omega_n' t]], \tag{2.7}$$

where

$$\boldsymbol{X} = \boldsymbol{x}(t) - \int_0^t \boldsymbol{u}_l(\boldsymbol{x}_l(t'), t')\, \mathrm{d}t', \tag{2.8}$$

and

$$\mathrm{d}\boldsymbol{x}_l(t')/\mathrm{d}t' = \boldsymbol{u}_l(\boldsymbol{x}_l(t'), t') \quad \text{given} \quad \boldsymbol{x}_l(t' = t) = \boldsymbol{x}.$$

$\boldsymbol{a}_n$, $\boldsymbol{b}_n$ and $\hat{\boldsymbol{\kappa}}_n$ are specified in §2.5.

The aspect of the interaction between modes that is correctly modelled by KS is simply the random advection of $\boldsymbol{u}_s$ by $\boldsymbol{u}_l$. But since $\boldsymbol{u}_l$ is non-uniform as well as being unsteady there is some deformation of the small-scale field by the large-scale motion $\boldsymbol{u}_l$ (see figure 4) and therefore in KSSM there is a small correlation between $\partial u_{l_i}/\partial x_j$ and $\partial u_{s_i}/\partial x_j$. This leads to small negative skewness, i.e. $\langle(\partial u_i/\partial x_i)^3\rangle < 0$. But the magnitude of the skewness is incorrect because KS does not simulate the dominant nonlinear interactions such as vortex stretching (Fung 1990).

Clearly the value of $\boldsymbol{u}_l$ used in the calculation of $\boldsymbol{u}_s$ is the same for all $k > k_c$, since we have assumed that all small eddies are carried along by the large eddies. This

would be a correct kinematical model if there were a gap in the spectrum, separating the wavenumber range into large and small scales. No attempt is made to smooth the transition between the large- and small-scale fields; this means that, as k_c varies, the frequency spectra and time correlations change (as described later). In reality, a high-wavenumber eddy is embedded in a continuous spectrum of eddies, and therefore a small 'small eddy' is swept by larger 'small eddies' as well as by energy-containing eddies. This effect can be neglected if the rate of change of the 'small eddies' is faster than the effect of sweeping by the larger 'small eddies'. Therefore for this form of KSSM the range of wavenumbers in the small-scale motion should be less than about 30 (for an inertial subrange). (The implications of this result are considered in §4.1).

Inertial Range Model: KSIM

We use a second model, KSIM, to investigate the relative motions of a pair of particles when the separations are small. In that case the motion is dominated by small scales and therefore in KSIM, we simulate only the small scales in a frame moving with the large eddies, using (2.2). As we show later, this approach is consistent with that of KSSM, for the small scales. The temporal structure of the small-scale field is studied in more detail than in KSSM by introducing a finite number (typically, $P_\omega = 1$ or 3) of frequencies (ω_{np}) at each wavenumber mode, so that each frequency mode is associated with a different wave vector.

2.2. *Continuity*

In KSSM the 'sweeping' of the small scales by the large scales is non-uniform in space, which leads to the gradients of small scales being affected. Then continuity is not explicitly satisfied. Taking the divergence of the velocity field yields terms such as $(\boldsymbol{a}_n \wedge \hat{\boldsymbol{\kappa}}_n)\cdot\boldsymbol{\nabla}(\boldsymbol{\kappa}_n\cdot\boldsymbol{X})$ which are non-zero because $\boldsymbol{X}$ – the displacement due to the large scales – is a function of $\boldsymbol{x}$ and $\boldsymbol{\kappa}$.

In order to satisfy continuity it is necessary in principle for the wavevector $\boldsymbol{\kappa}$ (and therefore frequency ω') to be a function of time (the details are given in Appendix A). This effectively models the rotation and distortion of the small-scale wavenumber motion by the large-scale velocity gradients. By neglecting the variation of $\boldsymbol{\kappa}$ with time the error in $\|\partial u_i/\partial x_i\|$ is proportional to $\partial^2 u_1/\partial x^2$.

The errors in the continuity equation were evaluated numerically (Fung 1990) and when normalized on $\|\partial u_{1_j}/\partial x_i\|$ were very small ($\lesssim 0.05$). By incorporating the correction to $\boldsymbol{\kappa}$ in the computation, it was found that the second-order statistics were only affected by about 10%.

In KSIM continuity is satisfied exactly because there is no non-uniform distortion of the small-scale field by the large scales. Note that where the two methods are compared there is a discrepancy of no greater than 10%.

2.3. *Eulerian spectra*

In both forms of KS, the energy spectrum of the simulated flow, $E_s(k)$, is approximated by the energy spectrum $E(k)$ of the turbulence that is to be simulated. In this paper we consider a function $E(k)$ (figure 2), which describes measurements of turbulent flows. For large-scale motion, $E(k) \propto k^4$, and for small-scale motion in the inertial range, $E(k) \propto k^{-\frac{5}{3}}$. This is the 'von Kármán spectrum' (Hinze 1975) whose properties were also discussed by Hunt (1973), namely

$$E_s(k) = E(k) = \gamma g_2 k^4/(g_1 + k^2)^{\frac{17}{6}} \quad \text{for} \quad 0 < k < k_\eta. \tag{2.9a}$$

It is assumed that the microscale motions ($k > k_\eta$) are simple straining motions caused by the eddies in the inertial range so that

$$E_s(k) = 0 \quad \text{for} \quad k > k_\eta. \tag{2.9b}$$

Note that $E(k)$ is normalized to give

$$\int_0^\infty E(k)\,\mathrm{d}k = \tfrac{1}{2}\langle \boldsymbol{u}(\boldsymbol{x},t)^2\rangle = \tfrac{3}{2}, \tag{2.10a}$$

and k is normalized on the integral lengthscale, derived from the energy spectrum (Monin & Yaglom 1975) by

$$L_{11} = \frac{3\pi}{4}\int_0^\infty k^{-1}E(k)\,\mathrm{d}k \Big/ \int_0^\infty E(k)\,\mathrm{d}k = 1. \tag{2.10b}$$

Thence the normalized numerical constants in (2.9) are given by

$$g_1 = \frac{\gamma\pi\Gamma^2(\frac{5}{6})}{\Gamma^2(\frac{1}{3})} = 0.558, \quad g_2 = \frac{55}{9}\frac{g_1^{\frac{5}{3}}}{\pi} = 1.196, \tag{2.11}$$

where in the limit of $k_\eta \to \infty, \gamma = 1$. For the case of $k_\eta = 50, \gamma = 1.1$.

In KSIM the energy spectrum in the inertial subrange is modelled without considering the small effects of intermittency on the spectrum (Kolmogorov 1962). Then

$$E_s(k) = \begin{cases} E(k) = \alpha_k \epsilon^{\frac{2}{3}} k^{-\frac{5}{3}} & \text{for} \quad k_c < k < k_\eta; \\ 0 & \text{for} \quad k < k_c \quad \text{and} \quad k > k_\eta, \end{cases} \tag{2.12}$$

and the Kolmogorov constant α_k is chosen to be 1.5 (Grant, Stewart & Moilliet 1962; Gibson 1963); ϵ is the rate of dissipation of kinetic energy per unit mass.

In KSIM the frequency dependence is modelled by assuming that the energy at each wavenumber is spread over a range of frequencies ($\sim \sigma_\omega(k)$) around a characteristic frequency $\varpi(k)$ in a Gaussian distribution (see figure 3), so that the small-scale wavenumber–frequency energy spectrum (in a frame advected by the large scales) is

$$\mathscr{E}_s(k,\omega) = E(k)\exp\{-\omega'^2/2\sigma_\omega^2(k)\}/(2\pi)^{\frac{1}{2}}\sigma_\omega(k), \tag{2.13}$$

where $\omega' = \omega - \varpi(k)$ and $\int_{-\infty}^{\infty} \mathscr{E}_s(k,\omega)\,\mathrm{d}\omega = E(k)$.

Since the simulation is for small-scale turbulence at high Reynolds number, $\varpi(k)$ and $\sigma_\omega(k)$ must both be determined by inertial-range scaling; we take $\varpi(k)$ and $\sigma_\omega(k)$ both equal to $\epsilon^{\frac{1}{3}}k^{\frac{2}{3}}$ (see Leslie 1973). Physically this correponds to the fact that smaller eddies change with time more quickly. (The decorrelation of a single wavenumber of a scalar field in turbulence on this timescale was measured in an ingenious experiment by Fermigier 1980.)

$E(k)$ and L_{11} are normalized as in (2.10).

2.4. *Maximum wavenumber k_η, cutoff wavenumber k_c, and Reynolds number*

The choice of k_η, the maximum wavenumber of the energy spectrum, determines both the Reynolds number and the integration time step. In a viscous flow at high Reynolds number, $k_\eta l \sim Re^{\frac{3}{4}}$ (Batchelor 1953), where $l \sim v^3/\epsilon$ is the lengthscale of the energy-containing eddies and $v^2 = \langle u_1^2\rangle$ is the velocity variance. Thus increasing k_η increases the Reynolds number of the simulation. At separations less than k_η^{-1}, the

velocity field is simply a uniform straining motion as assumed in many previous models (Batchelor 1959). Increasing k_η also decreases the time step which can be used in computing velocities and trajectories of fluid elements since the time step must be less than the inverse of the highest frequencies in the flow, and this increases the computational time. For KSSM we have used $k_\eta = 50$. In KSIM we have taken $k_c = 1$ and varied k_η between 10 and 400 to investigate the effect of varying the size of the inertial subrange.

In KSSM the cutoff wavenumber k_c marks the division between the large and the small eddies, and determines the proportion of the total energy assigned to each of the velocity fields. We have no *a priori* argument for determining k_c, but we have found that the Eulerian and Lagrangian autocorrelations, $R_{11}^E(\tau)$ and $R_{11}^L(\tau)$ are sensitive to k_c. At small τ the velocity fluctuations seen by a stationary observer are caused primarily by large-scale energetic eddies advecting small eddies past the observation point, whilst the fluctuating velocities experienced by a fluid element are due primarily to the time-evolution of the small-scale field. Since the large-scale eddies contain most of the energy, it follows that the Eulerian autocorrelation at small τ must decay faster than the Lagrangian autocorrelation (Shlien & Corrsin 1974; Tennekes 1975). That is, $R_{11}^L(\tau) > R_{11}^E(\tau)$ for small τ. This also follows from integrating the Eulerian and Lagrangian spectra to obtain the correlation functions at small time τ (see §4.14). Some experimental evidence and the theoretical argument of Reeks (1977) suggest that, at large τ, $R_{11}^E(\tau) > R_{11}^L(\tau)$. This implies that the curves must cross over (see figure 6 below). For small values of k_c, $R_{11}^E(\tau)$ exceeds $R_{11}^L(\tau)$ for all τ, and, for large values of k_c, $R_{11}^L(\tau)$ exceeds $R_{11}^E(\tau)$ for all τ. However, there is a narrow band of values for k_c in which the curves cross in the expected manner, and we have located k_c within this band, at $k_c = 5.0$ (somewhat arbitrarily). This apportions the energy between the large- and the small-scale fields in the ratio 5.8 to 4.2 (see Appendix B).

As one might expect, spatially determined variables – such as pressure and Lagrangian quantities – are not sensitive to the choice of k_c, but the Eulerian two-time correlation and frequency spectrum are sensitive to this assumption (which explains in part why the relation between Eulerian and Lagrangian correlations is not likely to be universal).

In KSIM, k_c represents the lowest wavenumber in the simulation; in all these computations it was set equal to 1.

To determine the Reynolds number we use the relationship $Re \sim [k_\eta \langle u_1^2 \rangle^{\frac{3}{2}}/\epsilon]^{\frac{4}{3}}$. (This estimate is only useful to indicate how Re varies. For low Re, it does not agree with the computations of Yeung & Pope 1989.) To estimate ϵ, we equate the energy in the small-scale field, whose energy spectrum is $E(k)$, to the energy in the equivalent range of the inertial-subrange spectrum, assuming

$$\int_{k_c}^{k_\eta} E_s(k)\,\mathrm{d}k = \int_{k_c}^{k_\eta} \frac{g_2 k^4}{(g_1 + k^2)^{\frac{17}{6}}}\,\mathrm{d}k = \tfrac{3}{2}\langle u_{1s}^2 \rangle = \alpha_k \epsilon^{\frac{2}{3}} \int_{k_c}^{k_\eta} k^{-\frac{5}{3}}\,\mathrm{d}k,$$

from which

$$\epsilon = \left[\frac{\langle u_{1s}^2 \rangle}{\alpha_k}\left(\frac{1}{k_c^{\frac{2}{3}}} - \frac{1}{k_\eta^{\frac{2}{3}}}\right)^{-1}\right]^{\frac{3}{2}}.$$

For KSSM, $k_c = 5.0$, $k_\eta = 50.0$ and $\langle u_{1s}^2 \rangle = 0.42$, giving $\epsilon = 1.066$ and a Reynolds number of 170. In KSIM, $k_c = 1.0$, $\langle u_{1s}^2 \rangle = 1.0$ and k_η varies between 10 and 400; the corresponding Reynolds numbers vary between 30 and 6390. Full details of all the parameters are given in table 1. (In KSIM the spectrum corresponds only to

Models	k_c	k_η	$\langle u_1^2 \rangle$	$\langle u_s^2 \rangle$	N_k	ϵ	L_{11}	Δt	Re
KSSM	5.0	50	0.58	0.42	38	1.066	1.00	0.0075	170
KSIM	1.0	10	—	1.00	35	0.783	1.17	0.0100	30
KSIM	1.0	100	—	1.00	300	0.585	0.99	0.0100	950
KSIM	1.0	400	—	1.00	1200	0.560	0.96	0.0025	6390

TABLE 1. Various parameters of simulations

the inertial subrange of the full turbulence spectrum. Thus, the total energy in the 'virtual' von Kármán spectrum that would contain KSIM is about double that in the inertial subrange and the virtual Reynolds number is $Re^* \approx 4Re$.)

2.5. *Determination of* k_n, $\boldsymbol{\kappa}_{mn}$, $\boldsymbol{a}_{mn}$ *and* $\boldsymbol{b}_{mn}$

The values of k_n have to be chosen by discretizing the wavenumber space into a finite number of modes. In KSSM, we use six modes for the large eddies ($0 < k_n < 5.0$) and 32 modes for the small eddies $5.0 \leqslant k_n \leqslant 50$. The wavenumbers are distributed as follows:

$$0 < k_n < 5.0, \quad k_n = 5.0 \times n/7, \qquad n = 1, 2, \ldots, 6;$$
$$5.0 \leqslant k_n \leqslant 50 \quad k_n = 5.0(50/5.0)^{(\frac{n-7}{31})}, \quad n = 7, 8, \ldots, 38.$$

A geometric progression has been chosen for the high wavenumbers of the small-scale motions to ensure that each mode carries approximately the same energy and to exclude the possibility of cyclic repetition of the velocity field.

In KSIM, the modes are distributed linearly according to the relationship

$$k_n = k_c + (k_\eta - k_c)(n-1)/(N_k - 1), \quad n = 1, \ldots, N_k,$$

in order to model the motion of particle pairs at small times and small separations, with a large number of modes at high wavenumber. The effects of different distributions of k_n on the statistics have been investigated by Malik (1991).

In any one realization, the unit vectors $\hat{\boldsymbol{\kappa}}_{mn}$ are chosen at random from a population distributed isotropically on the surface of a unit sphere. M_θ wavevectors $\boldsymbol{\kappa}_{mn}$ are chosen on each spherical shell of radius k_n but with differing and random directions. In both models the energy $E_s(k_n)$ at each wavenumber k_n is obtained by integrating the energy spectrum over a range of wavenumbers near k_n:

$$E_s(k_n) = \gamma \int_{k_n - \delta k/2}^{k_n + \delta k/2} E(k)\, \mathrm{d}k, \tag{2.14}$$

where $\delta k = (k_\eta - k_c)/(N_k - 1)$ and $\gamma = \int_0^\infty E(k)\, \mathrm{d}k \Big/ \int_0^{k_\eta} E(k)\, \mathrm{d}k$,

γ being a factor to compensate for the energy contained beyond k_η. The energy is assigned to each wavenumber $\boldsymbol{\kappa}_{mn}$ through the choice of $\boldsymbol{a}_{mn}$ and $\boldsymbol{b}_{mn}$.

For each mode to be independent and the velocity field to be non-divergent, statistically stationary, homogeneous and isotropic, it is necessary that:

$\boldsymbol{a}_{mn}, \boldsymbol{b}_{mn}, \boldsymbol{\kappa}_{mn}$ are independent of each other; (2.15*a*)

the distribution of $\boldsymbol{\kappa}_{mn}$ is isotropic; (2.15*b*)

$\langle (\boldsymbol{a}_{mn})_i \rangle = \langle (\boldsymbol{b}_{mn})_i \rangle = 0, \qquad i = 1, 2, 3;$ (2.15*c*)

$\langle (\boldsymbol{a}_{mn})_i (\boldsymbol{a}_{mn})_j \rangle = \langle (\boldsymbol{b}_{mn})_i (\boldsymbol{b}_{mn})_j \rangle = 0, \quad i \neq j;$ (2.15*d*)

$\langle (\boldsymbol{a}_{mn})_i^2 \rangle = \langle (\boldsymbol{b}_{mn})_i^2 \rangle, \qquad i = 1, 2, 3.$ (2.15*e*)

Then from (2.2), the energy at each wavenumber is given by

$$\langle u_n^2 \rangle = \sum_{m=1}^{M_\theta} \sum_{p=1}^{P_\omega} \langle |\boldsymbol{a}_{mnp} \wedge \hat{\boldsymbol{\kappa}}_{mn}|^2 \cos^2(\boldsymbol{\kappa}_{mn} \cdot \boldsymbol{x} + \omega_{np} t) \rangle + \langle |\boldsymbol{b}_{mnp} \wedge \hat{\boldsymbol{\kappa}}_{mn}|^2 \sin^2(\boldsymbol{\kappa}_{mn} \cdot \boldsymbol{x} + \omega_{np} t) \rangle. \quad (2.16)$$

We scale the velocity so that $\langle u_1^2 \rangle = \langle u_2^2 \rangle = \langle u_3^2 \rangle = 1$, and $\langle |\boldsymbol{u}|^2 \rangle = 3$. The energy spectrum $E(k) = \frac{3}{2}P(k)$, where $P(k)$ is the probability distribution of k-mode in k-space. Substituting in (2.15*a–e*), (2.16) reduces to

$$\langle u_n^2 \rangle = \frac{2}{3} \sum_{m=1}^{M_\theta} \sum_{p=1}^{P_\omega} \langle |\boldsymbol{a}_{mnp}|^2 \rangle = \frac{2}{3} \sum_{m=1}^{M_\theta} \sum_{p=1}^{P_\omega} \langle |\boldsymbol{b}_{mnp}|^2 \rangle = 3\gamma \int_{k_n - \delta k/2}^{k_n + \delta k/2} P(k)\, \mathrm{d}k. \quad (2.17)$$

Therefore $\boldsymbol{a}_{mnp}$ and $\boldsymbol{b}_{mnp}$ have to be chosen from distributions which satisfy (2.15*a–e*) and (2.17). We have used two different methods to do this.

In KSSM (where $P_\omega = 1$, $M_\theta = 1$ and $a_{mnp} = a_n$), the vectors $\boldsymbol{a}_n$ and $\boldsymbol{b}_n$ are picked independently from a three-dimensional Gaussian distribution with a zero mean vector and covariance matrix $\langle u_n^2 \rangle \delta_{ij}$.

In KSIM (where $P_\omega = 1$ or 3, $M_\theta = 1$), a_{mnp} and b_{mnp} are distributed isotropically on each sphere of radius k_n with $|\boldsymbol{a}_{mnp}| = |\boldsymbol{b}_{mnp}|$. Also, the energy $E_s(k_n)$ at wavenumber k_n is distributed equally over the P_ω frequency modes ω_{np}.

2.6. *Computational method*

For each run of the simulation, statistical quantities were obtained by taking the ensemble average of many realizations; most of the results in this paper were computed from 100 realizations of the velocity field. All the spectra in this paper are the average of 100 spectra. It is important to take the average of many realizations (rather than just allowing the simulation to run for a long time) because the initial choice of wave vectors, although random, determines much of the 'structure' of the velocity field.

The Eulerian velocity field is computed at fixed points. Lagrangian statistics are obtained by tracking fluid elements through the flow, by integrating the equation

$$\partial \boldsymbol{x}(t; \boldsymbol{a})/\partial t = \boldsymbol{u}[\boldsymbol{x}(t; \boldsymbol{a}), t], \quad \text{with} \quad \boldsymbol{x}(t = 0; \boldsymbol{a}) = \boldsymbol{a}, \quad (2.18)$$

using an extended Runge–Kutta scheme modified by Drummond *et al.* (1984) for KSSM and a second-order Taylor expansion for KSIM (Malik 1991).

For each realization of the velocity field the trajectories of 27 particles (in the case of KSIM, 27 pairs of particles) were computed simultaneously. The particles were released at the nodes of a $3 \times 3 \times 3$ lattice, spaced 6 integral lengthscales apart to minimize any initial correlation between the motion of the different particles. They were then tracked simultaneously for the required number of time steps and as many realizations as possible were generated, in order to produce accurate statistics.

The time step is determined by the need to track the motion of fluid elements at the smallest lengthscales. In KSSM the smallest wavelength is $2\pi/k_{38}$, which is about $0.12L_{11}$, where $L_{11}(= 1.0)$ is the integral lengthscale. We require Δt to be about 1/10th of the smallest timescale, which is of order $0.12L_{11}/\sigma_u$, i.e. $\Delta t < 0.012L_{11}/\sigma_u$. After some tests to ensure that the results were independent of Δt we chose $\Delta t = 0.0075$. The computations for KSSM were carried out in single precision on the Cray-2 computer at UKAEA Harwell Laboratories, and on the Cray XMP/48 at the Rutherford Appleton Laboratory for KSIM.

The method that we have developed is particularly useful and easy to implement

on parallel computers. Since we are investigating passive fluid particles, each processor in the parallel array can be assigned a particle (or pair of particles) and then the full efficiency of the parallel machine can be exploited. Some of the computations for KSIM were performed on an ICL Distributed Array Processor (DAP); this is a 64×64 array of processors, capable of running at about one third of the speed of the CRAY XMP/48. The method is also very well suited to exploit the vector processing capability of CRAY machines, and the maximum computational speed that has been obtained with KSIM on the CRAY XMP/48 is 160 MFLOPS. On this machine, an ensemble of 2700 particle pair trajectories for $k_\eta/k_c = 10$ took about 15 minutes CPU, and about 4 hours CPU for 1080 pairs at $k_\eta/k_c = 400$.

2.7. *Space–time structure of small eddies*

From the frequency–wavenumber relationships used in the algorithms of the simulations (KSSM and KSIM), it is possible to derive analytically the space–time correlation and structure functions in the limit of an infinite number of modes $N_k \to \infty$.

First consider how the Eulerian spatial structure function $D_{11}(r)$ is related to the spectrum and how it depends on the extent of the inertial range (k_η/k_c), where

$$D_{11}(r,0,0) = \langle [u_1(x+r,t) - u_1(x,t)]^2 \rangle. \tag{2.19}$$

For an infinite inertial subrange, $\eta_k \ll r \ll L$,

$$D_{11} = D_{11}^{\infty}(r,0,0) = C' \epsilon^{\frac{2}{3}} r^{\frac{2}{3}}, \tag{2.20}$$

where $C' = \frac{27}{55}\Gamma(\frac{1}{3})\alpha_k$ (Monin & Yaglom 1975). But with a finite extent of the inertial subrange of the spectrum $\phi_{11}(k_1)$ $(k_c < k < k_\eta)$,

$$\begin{aligned} D_{11}(r,0,0) &= 2\int_{k_c}^{k_\eta} \phi_{11}(k_1)(1-\cos k_1 r)\,\mathrm{d}k_1 \\ &\approx \frac{18\alpha_k}{55}\epsilon^{\frac{2}{3}} r^{\frac{2}{3}}[\tfrac{3}{2}\Gamma(\tfrac{1}{3}) - \tfrac{3}{4}(k_c r)^{\frac{4}{3}} - 3(k_\eta r)^{-\frac{2}{3}}]. \end{aligned} \tag{2.21}$$

The difference, defined by μ, between D_{11} for finite and infinite ranges of the inertial range is

$$\mu(r) = \frac{D_{11}^{\infty}(r) - D_{11}(r)}{D_{11}^{\infty}} = \frac{0.5(k_c r)^{\frac{4}{3}} + 2(k_\eta r)^{-\frac{2}{3}}}{\Gamma(\frac{1}{3})}.$$

For $k_\eta/k_c = 10$, in the range $0.05 < r < 0.15$ the maximum value of μ is about 40%, but as k_η/k_c is increased the difference decreases; for $k_\eta/k_c = 100$, 200 and 300 the maximum value of μ drops to 28%, 15% and 10% respectively, which can significantly reduce relative dispersion (see §4.2).

Now consider an observer moving with the large eddies and measuring the changes in the velocity (say on a scale k^{-1}, where k is the inertial subrange). It is assumed that the observer moves at a velocity $\boldsymbol{V}_0$ which is locally averaged over a scale l_0, where $k^{-1} \ll l_0 \ll L_0$. Thus $\boldsymbol{V}_0$ is independent of l_0. The structure function for the velocity at times t and $t+\tau$, measured in this randomly moving frame (which we call 'Eulerian–Lagrangian'), is determined by how small eddies change with lengthscales $k^{-1} \sim \tau v_k$ and velocity $v_k \sim \epsilon^{\frac{1}{3}} k^{-\frac{1}{3}}$, and vary with time, which is modelled by the ω_n' term in (2.7). Therefore, by scaling,

$$S_{11}^{\mathrm{EL}}(\tau) = \langle u_1(\boldsymbol{x},t)\, u_{11}(\boldsymbol{x}+\boldsymbol{V}_0 t, t+\tau)\rangle - \langle u_1(\boldsymbol{x},t)^2\rangle = 2\pi C^{\mathrm{EL}} \epsilon \tau. \tag{2.22}$$

If the observer actually travels with a fluid element (with displacement $\boldsymbol{\xi}(\tau) = \int_0^\tau \boldsymbol{u}(\boldsymbol{x}(t'), t')\,\mathrm{d}t'$), not only does the velocity change on this inertial-range timescale but the fluid element moves across the local velocity gradient. Since these gradients also scale on ϵ, the local Lagrangian structure function is

$$S_{11}^{\mathrm{L}}(\tau) = \langle u_1(\boldsymbol{x}, t)\, u_1(\boldsymbol{x}+\boldsymbol{\xi}, t+\tau)\rangle - \langle u_1(\boldsymbol{x}, t)^2\rangle = 2\pi C^{\mathrm{L}} \epsilon \tau \tag{2.23}$$

(Inoue 1951; Monin & Yaglom 1975). The above argument suggests that $C^{L} > C^{\mathrm{EL}}$.

To understand the difference between the Eulerian–Lagrangian and Lagrangian structure functions, consider two observers starting at $\boldsymbol{x}_0$ at time t_0 and moving with velocity $\boldsymbol{V}_0$. At time τ later the (EL) observer has moved a distance $\boldsymbol{V}_0 \tau$, while the (L) observer has moved a distance $\int_{t_0}^{t_0+\tau} \boldsymbol{u}\,\mathrm{d}t$; the distance l between the observers at time τ is of order $\epsilon^{\frac{1}{2}}\tau^{\frac{3}{2}}$ (see Appendix C). Therefore the difference between the root-mean-squared velocity of the observers is of order $l^{\frac{1}{3}}\epsilon^{\frac{1}{3}} \sim \epsilon^{\frac{1}{2}}\tau^{\frac{1}{2}}$, and so S_{11}^{L} cannot equal S_{11}^{EL}. But these two structure functions are of the same order, and the coefficients C^{L} and C^{EL} must also be of the same order.

For S_{11}^{EL} to have the high-Reynolds-number limit defined by (2.22) and for $E(k)$ to have the inertial-range form of $k^{-\frac{5}{3}}$, it is necessary that

$$\omega_n' = \lambda \epsilon^{\frac{1}{3}} k_n^{\frac{2}{3}}, \tag{2.24}$$

since in the inertial range the timescale is proportional to $\epsilon^{-\frac{1}{3}}k^{-\frac{2}{3}}$. In KSSM we choose $\lambda\epsilon = 1.0$, to give the correct forms for the Eulerian and Lagrangian correlations functions; λ is a constant of order unity, which can be related to the measurable coefficient C^{EL} (see Appendix C):

$$\lambda \approx 2C^{\mathrm{EL}}/\alpha_k. \tag{2.25a}$$

Thus for $\alpha_k = 1.5$, $\epsilon = 1.066$, $\lambda\epsilon^{\frac{1}{3}} = 1.0$, we have

$$C^{\mathrm{EL}} = 0.73. \tag{2.25b}$$

In KSIM, there is a Gaussian distribution of frequencies for each wavenumber. The theoretical value of C^{EL} is found to be 0.81 (Malik 1991).

Note that the change in the mean-square velocity of fluid elements over short times depends only on ϵ and the isotropic structure of the small scales, not on the critical wavenumber k_{c}. Note also that if the small-scale turbulence does not change with time as it is being advected by the large scales, then $\lambda = 0$, and S^{EL} and S^{L} would have the same form as S^{E}. This does not correspond with known results for small-scale turbulence (which are presented later).

The simulation KSSM is based on the assumption that the large-scale Gaussian velocity field $\boldsymbol{u}_1(\boldsymbol{x}, t)$ randomly advects the small-scale field $\boldsymbol{u}_{\mathrm{s}}(\boldsymbol{x}, t)$ (see figure 1). It follows from (2.7), (2.12) and (2.24) that at small scales ($k > k_{\mathrm{c}}$), the wavenumber–frequency energy spectrum has the approximate form

$$\mathscr{E}(k, \omega) = \tfrac{1}{2}E(k)\left[\frac{\exp\{-\frac{1}{2}\omega_+^2/(akU_0)^2\}}{(2\pi)^{\frac{1}{2}}akU_0} + \frac{\exp\{-\frac{1}{2}\omega_-^2/(akU_0)^2\}}{(2\pi)^{\frac{1}{2}}akU_0}\right], \tag{2.26}$$

where $U_0^2 = \frac{1}{3}\langle|\boldsymbol{U}|^2\rangle$, $\omega_+ = (\omega + \lambda\epsilon^{\frac{1}{3}}k^{\frac{2}{3}})$ and $\omega_- = (\omega - \lambda\epsilon^{\frac{1}{3}}k^{\frac{2}{3}})$. (The second terms in ω_+ and ω_- represent the decorrelation of the small scales as they are advected.) This expression follows exactly from the model if the large scales are uniform advective motions and the small scales do not change with time, in which case $a = 1$. When the frequency ω corresponds to large eddies advecting small eddies (i.e. $\omega \sim kU_0$), the

second terms in ω_+ and ω_- are much smaller than the first, and then, in a fixed frame, the spectrum has the form

$$\mathscr{E}(k,\omega) = E(k)\frac{\exp\{-\frac{1}{2}\omega^2/(akU_0)^2\}}{(2\pi)^{\frac{1}{2}}akU_0}. \tag{2.27}$$

The form of the model for $\mathscr{E}(k,\omega)$ in (2.27) agrees with the results of a direct numerical simulation of homogeneous turbulence by Hunt, Buell & Wray (1987). They found that the wavenumber–frequency energy spectrum had a similar form to that given in (2.27). However, they obtained a value of about 0.5, rather than 1.0, for the coefficient a. This was probably due to the low Reynolds number of the simulation, in which there was no inertial range. Chase (1970) showed that if $a = 1$ there is good agreement between wind tunnel experiments and the Eulerian autocorrelation derived from (2.27).

For high-Reynolds-number turbulence in the inertial subrange, the Eulerian frequency spectrum $\phi_{11}^{\mathrm{E}}(\omega)$ of one component of velocity, u_1 say, measured at a point (moving with the mean flow) is determined by the large-scale advection of eddies past the observer, and has the form (Tennekes 1975)

$$\phi_{11}^{\mathrm{E}}(\omega) = \int_0^\infty \mathscr{E}(k,\omega)\,\mathrm{d}k = C^{\mathrm{E}}(\epsilon U_0)^{\frac{2}{3}}\omega^{-\frac{5}{3}} \quad \text{for} \quad k_\eta^{\frac{2}{3}}\epsilon^{\frac{1}{3}} \gtrsim \omega \gtrsim k_{\mathrm{c}}^{\frac{2}{3}}\epsilon^{\frac{1}{3}}, \tag{2.28}$$

where U_0 is the r.m.s. velocity of the turbulence. If the large scales are isotropic and Gaussian and the Reynolds number is large enough for there to be a large separation in scales between the energy-containing eddies and those in the inertial subrange, then C^{E} should be independent of the large scales and should be a universal constant.

In the inertial subrange where $E(k) = \alpha_k\,\epsilon^{\frac{2}{3}}k^{-\frac{5}{3}}$, it follows that, by integrating (2.26) analytically or numerically, the frequency spectrum at a point has the form given in (2.28), and the constant C^{E} is

$$C^{\mathrm{E}} = 0.8 \quad \text{for} \quad a = 1.0. \tag{2.29}$$

Since as $Re \to \infty$ random advection takes place on all scales (not just for $k > k_{\mathrm{c}}$), in a real turbulent flow, U_0 in (2.28) can be replaced by $\langle u_1^2\rangle^{\frac{1}{2}}$.

2.8. *Pressure field associated with KS velocity fields*

From any simulation of a velocity field it is possible to compute the pressure field, and kinematic simulation is no exception. In §5, we compare our simulations with theoretical predictions.

For the scale of motion consider here, the pressure is related to the velocity field by the equation

$$(1/\rho)\,\boldsymbol{\nabla} p = -\partial\boldsymbol{u}/\partial t - (\boldsymbol{u}\cdot\boldsymbol{\nabla})\,\boldsymbol{u}. \tag{2.30}$$

Decomposing the velocity and pressure fields into large- and small-scale fields, we obtain

$$-(1/\rho)\,\boldsymbol{\nabla}(p_{\mathrm{l}}+p_{\mathrm{s}}) = \partial(\boldsymbol{u}_{\mathrm{l}}+\boldsymbol{u}_{\mathrm{s}})/\partial t + (\boldsymbol{u}_{\mathrm{l}}+\boldsymbol{u}_{\mathrm{s}})\cdot\boldsymbol{\nabla}(\boldsymbol{u}_{\mathrm{l}}+\boldsymbol{u}_{\mathrm{s}}). \tag{2.31}$$

Averaging the pressure over a small region in space, with characteristic length L, yields the equation for the large-scale pressure field:

$$-(1/\rho)\,\boldsymbol{\nabla} p_{\mathrm{l}} = \partial\boldsymbol{u}_{\mathrm{l}}/\partial t + \boldsymbol{u}_{\mathrm{l}}\cdot\boldsymbol{\nabla}\boldsymbol{u}_{\mathrm{l}} + \langle\langle \boldsymbol{u}_{\mathrm{s}}\cdot\boldsymbol{\nabla}\boldsymbol{u}_{\mathrm{s}}\rangle\rangle, \tag{2.32}$$

where $\langle\langle\ \rangle\rangle$ denotes the spatial average, $\langle\langle \boldsymbol{u}_{\mathrm{s}}\rangle\rangle = 0$ and $\langle\langle \boldsymbol{u}_{\mathrm{l}}\rangle\rangle = \boldsymbol{u}_{\mathrm{l}}$. Subtracting this from (2.31), yields the small-scale pressure field:

$$-(1/\rho)\,\boldsymbol{\nabla} p_{\mathrm{s}} = \partial\boldsymbol{u}_{\mathrm{s}}/\partial t + \boldsymbol{u}_{\mathrm{s}}\cdot\boldsymbol{\nabla}\boldsymbol{u}_{\mathrm{s}} - \langle\langle \boldsymbol{u}_{\mathrm{s}}\cdot\boldsymbol{\nabla}\boldsymbol{u}_{\mathrm{s}}\rangle\rangle + \boldsymbol{u}_{\mathrm{s}}\cdot\boldsymbol{\nabla}\boldsymbol{u}_{\mathrm{l}} + \boldsymbol{u}_{\mathrm{l}}\cdot\boldsymbol{\nabla}\boldsymbol{u}_{\mathrm{s}}. \tag{2.33}$$

The large- and small-scale pressure fields can be computed from the known Fourier coefficients for the large- and small-scale fields. This is a double sum over all possible wavenumber pairs, and is computationally expensive. Details are given by Fung (1990).

3. Simulation results for an Eulerian field

3.1. *One-point statistical test of the flow field*

Various statistical quantities have been computed from the simulated flow field in order to check that it has the desired properties. Using a large number of realizations ($\geqslant 100$, i.e. more than 2700 particle trajectories since 27 particle trajectories are simulated in each realization) of KS, it is found that

$(a)\langle \boldsymbol{u}(\boldsymbol{x},t)\rangle \to 0 \pm 0.03$;

$(b)\langle \boldsymbol{x}(t)\rangle \to 0 \pm 0.02$;

$(c)\langle u_i^2(\boldsymbol{x},t)\rangle \to 1 \pm 0.05$, $i = 1,2,3$, for all $\boldsymbol{x}$ and t (isotropic, homogenous and stationary).

Most experiments and computations of homogeneous, isotropic turbulence have shown that the velocity at one point has an approximately normal distribution. The moments of order three and higher (e.g. skewness and flatness) are often used as indicators. The computed flatness factors $\langle u_i^4\rangle/3\langle u_i^2\rangle^2$ and $\langle u_i^6\rangle/7.5\langle u_i^2\rangle^3$ converge to the values of 1.0 ± 0.02 and 2.0 ± 0.3 respectively, and the skewness factors $\langle u_1^3\rangle/\langle u_1^2\rangle^{\frac{3}{2}}$ and $\langle u_1^5\rangle/\langle u_1^2\rangle^{\frac{5}{2}}$ converge to the value 0.0 ± 0.05. The mean values are all equal to those for Gaussian distributions.

One-dimensional wavenumber spectra ($0 < k < 75$) $\phi_{ii}(k_1)$, where $i = 1,2,3$ at $t = 0$ have been computed from KSSM, they have the theoretical slope of $-\frac{5}{3}$ in the range $2 < k < 70$ and a sharp cutoff at $k_1 = 75$ since there is no energy at wavenumbers higher than 75 at the start of the simulation. After about ten integral timescales, the typical time of simulation, there is a small difference between the spectrum $\phi_{ii}(k_1,t)$ and its initial form $\phi_{ii}(k_1,0)$ for $k \gtrsim 30$ because a small amount of energy is transferred to wavenumbers higher than $k_1 = 75$ from wavenumbers lying between 30 and 75, caused by the non-uniform advection of the small-scale eddies by the large-scale eddies. There is no transfer of energy in the KSIM simulation which has no advection. Thus over the time period considered here, for large scales and over most of scales in the inertial range and larger, both simulations are stationary.

3.2. *The spatial structure function*

The structure function D_{11} (as defined in (2.20)) was computed for both KSSM and KSIM and the results are plotted in figure 5. The straight line portion has a slope of approximately $\frac{2}{3}$ and the constant C' is equal to 1.7; this should be compared with the experimental value of 2.0 ± 0.1 (Townsend 1976). The theoretical correction terms in (2.21) for finite extent of the inertial range are consistent with differences between the asymptotic theory and simulations in figure 5. See also Anselmet *et al.* (1984), Van Atta & Chen (1970).

3.3. *Eulerian autocorrelation and frequency spectra*

The autocorrelation of the fluctuating velocity at a point, $R_{11}^{\mathrm{E}}(\tau)$, is presented in figure 6. It is positive for all τ. The integral timescale T^{E} is defined as $\int_0^\infty R_{11}^{\mathrm{E}}(\tau)\,\mathrm{d}\tau$ (Taylor 1921) but it can be difficult to calculate this from a record of finite duration (Comte-Bellot & Corrsin 1971) so we define it as the value of τ at which R_{11}^{E} falls to 1/e of its value at $\tau = 0$. On this basis we obtain $T^{\mathrm{E}} = 0.8$.

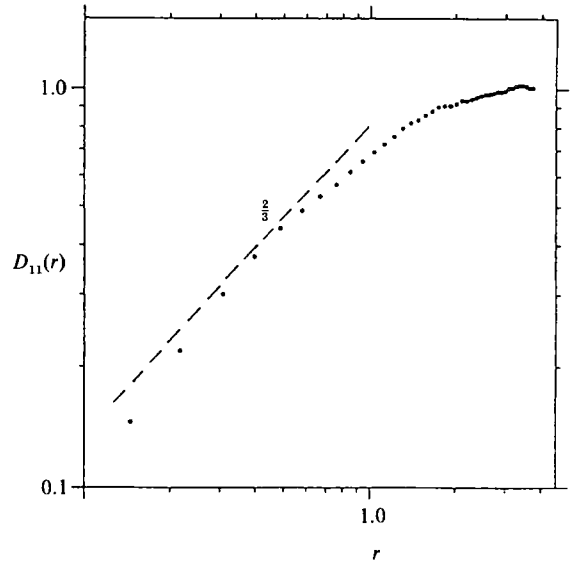

FIGURE 5. The structure function $D_{11}(r)(=C'\epsilon^{\frac{2}{3}}r^{\frac{2}{3}})$ showing a $\frac{2}{3}$ slope over a limited range.

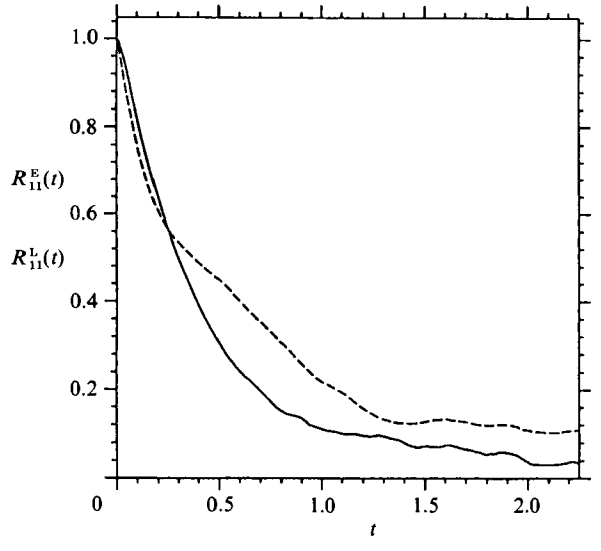

FIGURE 6. The Eulerian $R_{11}^{E}(\tau)$ (----) and Lagrangian $R_{11}^{L}(\tau)$ (——) autocorrelation functions, there is a crossover at $\tau \approx 0.2$.

The grid turbulence measurements of Favre, Gaviglio & Dumas (1957) and numerical simulations of Moin & Moser (1989) for channel flow, Squires (1990) for decaying grid turbulence and Hunt *et al.* (1987) for stationary, homogeneous turbulence (where there is a significant component of turbulence at zero frequency) indicate that if T_E is normalized in terms of the r.m.s. velocity and the integral lengthscale L_{11} it is equal to the coefficient β^E defined by

$$T_E = \beta^E L_{11}/\langle u_1^2\rangle^{\frac{1}{2}}, \tag{3.1}$$

where β^E varies between about 0.5 and 1.0 depending on the structure of turbulence.

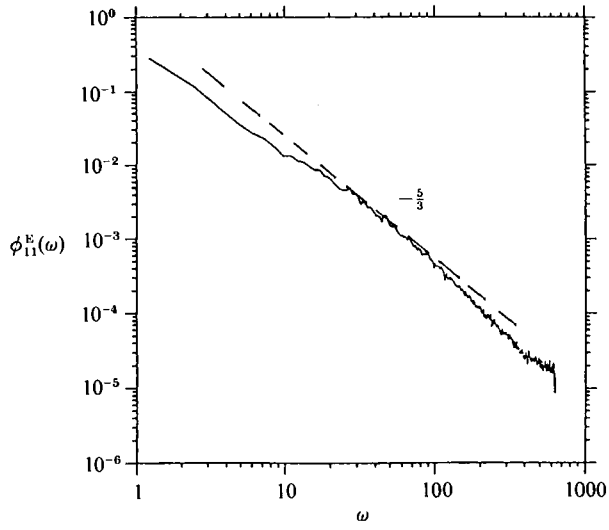

FIGURE 7. Average Eulerian frequency spectrum $\phi_{11}^{E}(\omega)\,(= C^{E}(\epsilon U_0)^{\frac{2}{3}}\omega^{-\frac{5}{3}})$ with a $-\frac{5}{3}$ slope.

Snyder & Lumley (1971) inferred a value of $\beta^{E} \approx 3$ by interpreting their heavy-particle correlations as representative of Eulerian correlations and light-particle results as representative of Lagrangian correlations. It is interesting that in our simulations of high-Reynolds-number turbulence, for different values of k_c (2.5, 5.0 and 10.0) β^{E} was found to vary, in this case between 0.5 and 0.9, which are somewhat less than the previous quoted values (see table 2 below). In our simulation the larger values of k_c correspond to relatively more energy being in the large-scale sweeping motion $\boldsymbol{u}_1$ and this explains why β^{E} increases as k_c increases.

Figure 7 shows the computed form of the Eulerian frequency spectra $\phi_{11}^{E}(\omega)$. Over most of the inertial range ($10 < k < 50$), the slope is equal to $-\frac{5}{3}$, showing that the advection has a much greater effect on the frequency spectrum for a fixed observer than the decorrelation of the small eddies as they are advected by the large scales. The computed value of C^{E} is 0.82. This is close to the value of 0.78 derived in (2.29) in the asymptotic limit for very small-scale turbulence, whose advection by the large scales does not depend on their spatial structure. For other statistics this is an inappropriate assumption, as we show in §4.

3.4. *How can we quantify 'Structure' in a flow?*

The identification of certain significant regions in each realization of flow can provide an important method for analysing the dynamics of the flow and also provides a criterion for assessing approximate models of the flow fields.

Following Perry & Chong (1987) and Wray & Hunt (1990), the flow structure can be objectively characterized in terms of the local values of the deformation tensor $u_{i,j}$, (specifically the second invariant $\mathrm{II} = (\partial u_i/\partial x_j)(\partial u_j/\partial x_i)$ of the velocity field) and the pressure p. The flow is divided into high-vorticity regions, corresponding to regions of high swirl where $\mathrm{II} < -\mathrm{II}_{\mathrm{rms}}$, $p < -p_{\mathrm{rms}}$, convergence regions (C), where $\mathrm{II} > \mathrm{II}_{\mathrm{rms}}$, $p > p_{\mathrm{rms}}$, and streaming regions (S) where $-\mathrm{II}_{\mathrm{rms}} \leqslant \mathrm{II} \leqslant \mathrm{II}_{\mathrm{rms}}$ and $u^2 \geqslant u_{\mathrm{rms}}^2$.

Using these flow zones as a criterion kinematic simulation has been compared to the results of direct numerical simulations by Fung *et al.* (1991). It is shown that KS can approximately (and 'cheaply') simulate the instantaneous flow structure in

homogeneous and isotropic turbulence; but the zonal analysis also shows that the shapes of certain key features which are determined by the local dynamics are not correctly simulated. In particular, elongated vortex tubes and sheets (found in recent simulations and experiments by Vincent & Meneguzzi 1991 and by Schwarz 1990) are not sufficiently elongated (Fung *et al.* 1991).

4. Lagrangian statistics

4.1. *One-point Lagrangian statistics*

4.1.1. *Lagrangian integral timescale*

The Lagrangian integral timescale characterizes the velocity and displacement of a fluid particle as it moves through a turbulent flow field. It is defined as

$$T_{\mathrm{L}} = \int_0^\infty R_{11}^{\mathrm{L}}(\tau)\,\mathrm{d}\tau,$$

and can either be derived from the Lagrangian autocorrelation function $R_{11}^{\mathrm{L}}(\tau)$, defined as

$$R_{11}^{\mathrm{L}}(\tau) = \frac{\langle u_i(\boldsymbol{x}(t),t)\,u_i(\boldsymbol{x}(t+\tau),t+\tau)\rangle}{(\langle u_i^2(\boldsymbol{x}(t),t)\rangle\,\langle u_i^2(\boldsymbol{x}(t+\tau),t+\tau)\rangle)^{\frac{1}{2}}}, \tag{4.1}$$

or can more easily be obtained from the mean-square displacement $\langle x^2(t)\rangle$ of fluid elements, since if the statistics of the turbulence are stationary, for $t \gg T_{\mathrm{L}}$ (Taylor 1921)

$$\langle \boldsymbol{x}^2(t)\rangle \approx 2\langle \boldsymbol{u}^2(x,t)\rangle\, T_{\mathrm{L}}\, t. \tag{4.2}$$

When $t \gtrsim T_{\mathrm{L}}$, the slope of graphs of $\log\{\langle \boldsymbol{x}^2(t)\rangle\}$ are within 5% of the theoretical value of 1.0. From the graph we estimate that $T_{\mathrm{L}} \approx 0.5$. A similar set of computations for KSIM (which has a different large-scale structure) shows that $T_{\mathrm{L}} \to 0.3$ as $k_\eta/k_{\mathrm{c}} \to \infty$ (see Malik 1991).

Just as with the Eulerian timescale T_{E}, it is constructive to express T_{L} in terms of the non-dimensional constant β^{L}, defined as in (3.1) by

$$T_{\mathrm{L}} = \beta^{\mathrm{L}} L_{11}/\langle u_i^2\rangle^{\frac{1}{2}}. \tag{4.3}$$

Experiments and simulations indicate that $\beta^{\mathrm{L}} \approx 1$ for grid turbulence (Snyder & Lumley 1971), and boundary-layer turbulence (Durbin & Hunt 1980). However we obtain a value of $\beta^{\mathrm{L}} \approx 0.5$ in high-Reynolds-number turbulence. We have also tested the sensitivity of β^{L} to the critical wavenumber k_{c} and the results appear in table 2; these show that β^{L} is not sensitive to k_{c}. The ratio of T_{L} to T_{E} is given in table 2 and the ratio shows a dependence on k_{c} because T_{E} depends on k_{c}. From KSIM, $T_{\mathrm{L}}/T_{\mathrm{E}} \approx 0.6$ at high Reynolds number. In a recent direct numerical simulation of isotropic turbulence (Re_λ in the range 38–93) Yeung & Pope (1989) found $T_{\mathrm{L}}/T_{\mathrm{E}} \approx 0.8$.

4.1.2. *Lagrangian spectrum in the inertial subrange*

Inoue (1951) applied Kolmogorov's dimensional scaling analysis to predict the form of the Lagrangian velocity spectrum for frequencies in the inertial subrange. He obtained

$$\phi_{11}^{\mathrm{L}}(\omega) = C^{\mathrm{L}}\epsilon\omega^{-2} \quad \text{for} \quad \omega_{\mathscr{L}} \ll \omega \ll \omega_\eta, \tag{4.4}$$

where $\omega_{\mathscr{L}}$ refers to the energy-containing part of the Lagrangian spectrum, and $\omega_\eta (= (\epsilon/\nu)^{\frac{1}{2}})$ is the Kolmogorov frequency. C^{L} is a universal constant of order 1,

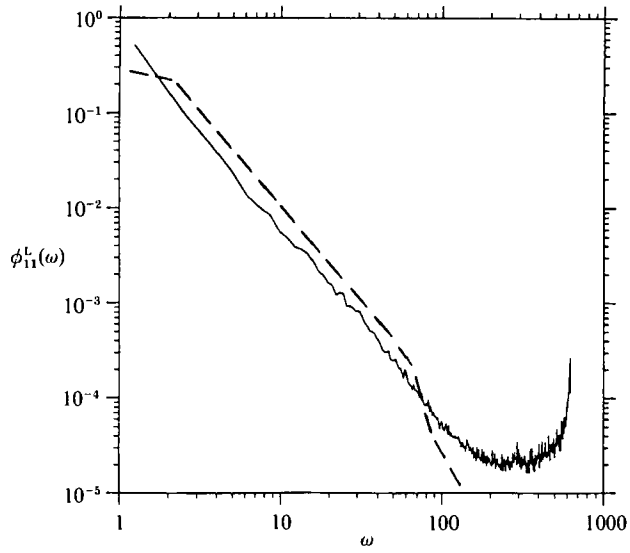

FIGURE 8. Average Lagrangian spectrum $\phi_{11}^{L}(\omega)(= C^{L}\epsilon\omega^{-2})$ with a -2 slope with $k_\eta/k_c = 50$. ——, KSSM; ---, KSIM.

k_c/L	k_η/L	ϵ	u_1^2/u_s^2	$u_1^3 k_c/\epsilon$	$1/\beta^{L}$	$1/\beta^{E}$	T_L/T_E
2.5	50.0	0.7190	0.6393	4.4004	1.80	2.00	1.11
5.0	50.0	0.8215	1.3810	14.5706	1.92	1.25	0.65
10.0	50.0	0.7850	2.8961	42.4210	2.17	1.14	0.53
1.0	100.0	0.5850	—	—	—	—	0.60

TABLE 2. Variation of Eulerian and Lagrangian timescales with different ratios of the energy of large-scale to small-scale turbulence

although its exact value is uncertain. One of the purposes of this simulation is to verify that $\phi_{11}^{L}(\omega) \propto \omega^{-2}$ and to obtain an estimate for C^{L}.

The Lagrangian spectrum $\phi_{11}^{L}(\omega)$ computed using both KSSM and KSIM are plotted in figure 8 with $k_\eta/k_c = 50$. Over the inertial range the spectrum is a straight line with a slope of -2; the deviation at high frequencies is caused by noise from the numerical integration rather than the energy transfer from large eddies to small eddies since the form of the spatial spectrum does not evolve with time (see §3.3). From the graph, $C^{L} \approx 0.79$ for KSSM; for KSIM we obtained $C^{L} \approx 0.81$. These are consistent with measurements by Hanna (1981) in the atmospheric boundary layer using balloons and tetroons, which suggest that $C^{L} = 0.6 \pm 0.3$. From their simulation at $R_\lambda = 90$, Yeung & Pope (1989) predicted that C^{L} should be slightly greater than 0.64.

When k_η/k_c increases much above 50, in the KSIM simulations (Malik 1991) the slope of the Lagrangian spectrum systematically increases above -2 and for $k_\eta/k_c > 100$, it tends to a slope of -1.8. This is to be expected because with such a long inertial range the sweeping of the small inertial-range eddies by the large inertial-range motion should be included. Without this effect the particles are changing their velocity as a result of large eddies advecting particles past fixed small eddies; this leads to an increase in $\phi_{11}^{L}(\omega)$ and hence a slope of $-\frac{5}{3}$. This is consistent with the frozen turbulence described below.

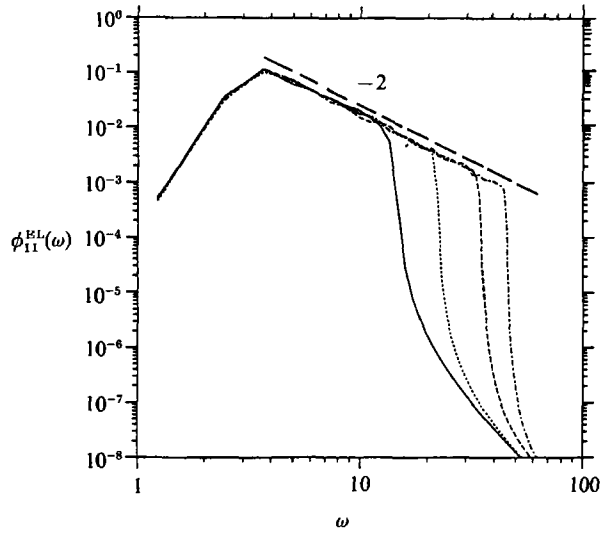

FIGURE 9. Average Eulerian–Lagrangian spectrum $\phi_{11}^{EL}(\omega)(=C^{EL}\epsilon\omega^{-2})$ with a -2-slope with $k_c = 5$ and: ——, $k_\eta = 50$ (32 modes); ....., $k_\eta = 100$ (64 modes); – – – –, $k_\eta = 200$ (128 modes); —·—·—, $k_\eta = 300$ (256 modes).

Taking the Fourier transform of the spectrum (4.4) yields the autocorrelation

$$R_{11}^{L}(\tau) = \int_{-\infty}^{\infty} \phi_{11}^{L}(\omega)\, e^{i\omega\tau}\, d\omega = \langle u_1^2 \rangle - \pi C^{L}\epsilon\tau \quad \text{for} \quad \tau_L \ll \tau \ll T_L. \tag{4.5}$$

From the measurements of the velocity of particles moving through the simulated field, the autocorrelation was evaluated directly. Using (4.5) it was found that $C^L \approx 0.75$ which agrees with the computation from the spectrum.

Note how at small times, $R^L(\tau) > R^E(\tau)$, which is consistent with (4.5).

4.1.3. *The 'Eulerian–Lagrangian' spectrum*

In §2.7 we calculated the Eulerian–Lagrangian autocorrelation in a frame moving with the large eddies. The Eulerian–Lagrangian spectrum $\phi_{ij}^{EL}(\omega)$ can be obtained from the Fourier transform of this autocorrelation:

$$\phi_{11}^{EL}(\omega) = C^{EL}\epsilon\omega^{-2}. \tag{4.6}$$

Using KSSM we have computed $\phi_{11}^{EL}(\omega)$ for different values of k_η, and these are shown in figure 9. The extent of the range where the 'slope' is -2 increases with k_η. From the graph we estimate $C^{EL} \approx 0.76$. This is close to the theoretical result of (2.25) that $C^{EL} = 0.73$.

Note that C^{EL} is close to the coefficient for the Lagrangian spectrum (0.8). There is no theoretical reason why they should be exactly equal. A slightly higher result for C^{EL} was obtained from KSIM, namely $C^{EL} = 0.81$; this is even closer to the value of C^L. This is an important finding because it suggests that the Eulerian wavenumber–frequency spectrum can be used to give a very good approximation to the Lagrangian spectrum. (This should be tested by direct numerical simulation.)

4.1.4. *'Frozen-Lagrangian' spectra*

To what extent do the Lagrangian spectra and the time structure function depend on the unsteadiness of the velocity field? We have simulated 'frozen turbulence' (where there is no time dependence so that $\boldsymbol{u}(\boldsymbol{x}) = \boldsymbol{u}_l(\boldsymbol{x}) + \boldsymbol{u}_s(\boldsymbol{x})$) and have computed

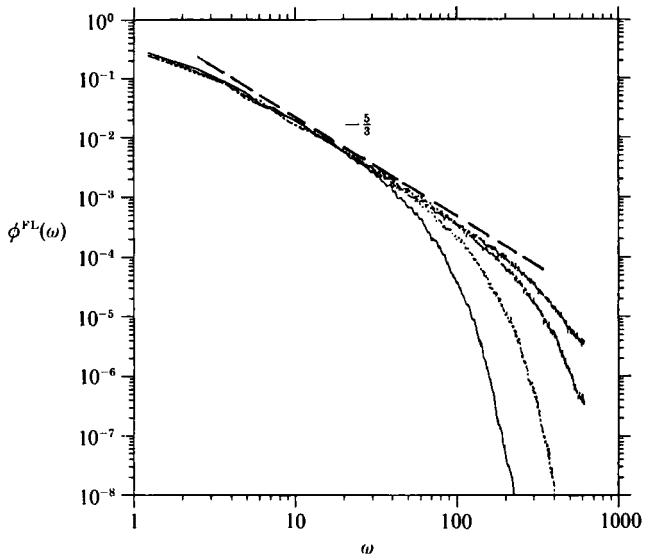

FIGURE 10. Average frozen Lagrangian spectrum $\phi^{FL}(\omega)(=C^{FL}(\epsilon u_1)^{\frac{2}{3}}\omega^{-\frac{5}{3}})$, with a $-\frac{5}{3}$ slope. Parameter values as figure 9.

the Lagrangian spectrum $\phi^{FL}(\omega)$ for different sizes of inertial subrange. The spectra are shown in figure 10. The straight line portions of the spectra have a slope of $-\frac{5}{3}$ (and the range increases as k_η increases) showing that the velocity fluctuations of particles are caused by being swept through the small eddies by the large eddies. This does not happen if the small eddies are themselves swept by the large eddies. The energy in this spectrum is lower than in the Eulerian spectrum $\phi_{11}^{E}(\omega)$ for all frequencies, but higher than in the corresponding Lagrangian spectrum $\phi_{11}^{L}(\omega)$ at high frequencies, so that the relative importance of high-frequency components in fluctuating fluid particle velocity is less than for the velocity fluctuations at a fixed point; this is an important effect for the turbulent interface problem (Carruthers & Hunt 1986). Therefore to simulate the high-frequency velocity and displacement of particles it is necessary to simulate the time dependence of the velocity field. (Note that Kolmogorov 1941 (in a footnote) suggested that this does not affect the statistics of the small-scale flow; our results are not consistent with this idea.)

We also computed the Lagrangian velocity spectrum $\phi_{11}^{FL,s}(\omega)$ for frozen small-scale turbulence $\boldsymbol{u}_s(\boldsymbol{x})$ (in a frame moving with the large scales), with the time evolution of the small scales 'turned off', i.e. $\omega_n' = 0$.

From dimensional arguments or analysis

$$\phi_{11}^{FL} = C^{FL}(\epsilon u_1)^{\frac{2}{3}}\omega^{-\frac{5}{3}} \quad \text{and} \quad \phi_{11}^{FL,s} = C^{FL,s}(\epsilon u_{1s})^{\frac{2}{3}}\omega^{-\frac{5}{3}},$$

where from KSSM the computed results are $C^{FL} = 0.41$ and $C^{FL,s} = 0.37$ and from KSIM, $C^{FL,s} = 0.33$.

4.2. *Relative displacement of pairs of particles*

4.2.1. *Brief overview of previous results*

To model processes such as mixing and combustion we need statistical information about the relative displacement of particle pairs in a turbulent flow (Thomson 1987).

The general problem is to determine how the average separation $\langle\Delta(t)\rangle$ of a pair of fluid elements at $\boldsymbol{x}_1(t)$ and $\boldsymbol{x}_2(t)$ varies with time, where $\Delta(t) = (\Delta_1^2+\Delta_2^2+\Delta_3^2)^{\frac{1}{2}} = |\boldsymbol{x}_1(t)-\boldsymbol{x}_2(t)|$ and the initial separation is denoted by Δ_0 (figure 11*a*).

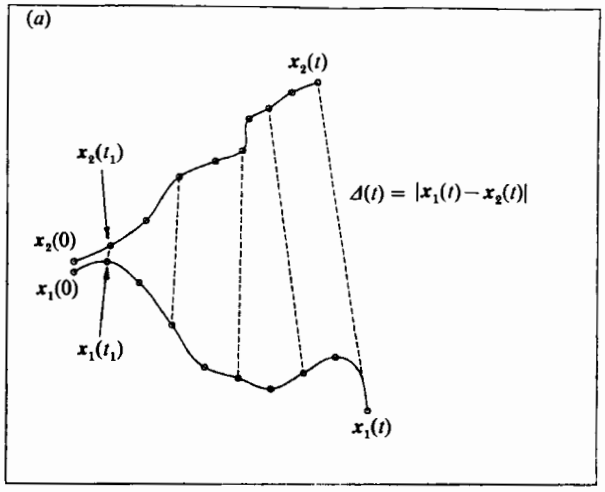

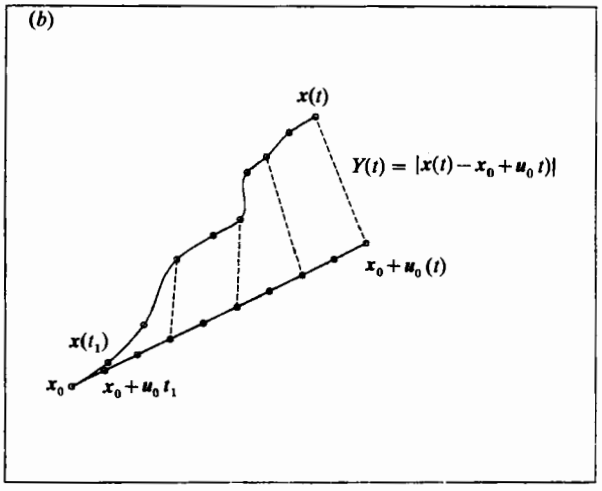

FIGURE 11. (*a*) Particles 1 and 2 released at time $t = 0$ from $\boldsymbol{x}_1(0)$ and $\boldsymbol{x}_2(0)$. Initial separation $\Delta_0 = |\boldsymbol{x}_1(0) - \boldsymbol{x}_2(0)| \ll \eta$. (*b*) The separation $Y(t)$ of a particle in a frame of reference which is moving with initial velocity $\boldsymbol{u}_0$.

Obukhov (1941) considered the motion of particle pairs at separations within the inertial subrange and proposed that the value of ϵ determines $\langle \Delta^2 \rangle$ over this scale, which (when $L^2 \gg \langle \Delta^2 \rangle \gg \Delta_0^2$) leads to the result

$$\langle \Delta^2(t) \rangle - \Delta_0^2 = G_\Delta \epsilon t^3. \tag{4.7}$$

Although there have been several experiments that are consistent with the theoretical t^3 dependence of Δ^2, the constant G_Δ has never been measured with reliable accuracy because of the difficulty of estimating the energy dissipation rate ϵ. Only Tatarski (1960) has estimated G_Δ experimentally. He obtained values for $G_\Delta = 0.06$, 0.17 or 0.45, but the errors could be considerable (Malik 1991).

Novikov (1963) obtained an estimate for G_Δ by considering the related problem of the displacement of a fluid element relative to its initial trajectory, and we refer to

k_η	N_k	γ	γ_y	C	C_Y	$G_\Delta(=C/\epsilon)$	$G_Y(=C_Y/\epsilon)$
10	35	1.60 ± 0.20	2.60 ± 0.50	1.28	1.80	1.64 ± 0.10	2.3 ± 0.50
25	80	1.90 ± 0.15	2.60 ± 0.10	0.57	1.99	0.87 ± 0.10	3.0 ± 0.20
50	150	2.30 ± 0.03	2.65 ± 0.20	0.27	2.00	0.44 ± 0.10	3.3 ± 0.20
100	300	2.60 ± 0.02	2.68 ± 0.10	0.13	2.22	0.23 ± 0.10	3.8 ± 0.30
200	600	2.78 ± 0.01	2.78 ± 0.05	0.09	2.33	0.16 ± 0.07	4.1 ± 0.30
300	900	2.95 ± 0.01	2.80 ± 0.05	0.06	2.53	0.11 ± 0.05	4.5 ± 0.40
400	1200	2.97 ± 0.01	2.83 ± 0.05	0.06	2.69	0.10 ± 0.05	4.8 ± 0.50

TABLE 3. Statistics of relative diffusion derived from two-particle simulations using KSIM

these as *difference* statistics. The particle is initially at $\boldsymbol{x}_0$, with velocity $\boldsymbol{u}_0$. An imaginary particle is also released with identical initial conditions, but it moves in a straight line with velocity $\boldsymbol{u}_0$, unaffected by the dynamics of the flow (figure 11*b*). At a later time the distance and velocity difference between the real and imaginary particle are

$$Y(t) = |\boldsymbol{x}(t) - (\boldsymbol{x}_0 + \boldsymbol{u}_0 t)|, \quad \boldsymbol{V}(t) = \boldsymbol{u}(\boldsymbol{x}, t) - \boldsymbol{u}_0. \tag{4.8a}$$

From (4.2) and (4.5), the variance of Y of a particle has been calculated from the Lagrangian autocorrelation function $R^{\mathrm{L}}(\tau)$ for different times after release in the ranges $t/\tau_\eta \ll 1$, $1 \ll t/\tau_\eta \ll T_{\mathrm{L}}/\tau_\eta$ and $1 \ll t/T_{\mathrm{L}}$, namely

$$\langle Y^2(t)\rangle = (u_0^2/3\tau_{\mathrm{L}}^2)\, t^4,\ G_Y \epsilon t^3 \quad \text{and} \quad 2u_0^2 T_{\mathrm{L}} t, \tag{4.8b}$$

respectively, where $G_Y = 2\pi C^{\mathrm{L}}$ and $u_0^2 = \langle \boldsymbol{u}^2 \rangle$. Novikov (1963) used these results to estimate $\langle \Delta^2 \rangle$ by assuming that accelerations are only correlated over distances much smaller than η and for times much smaller than τ_η. Therefore two particles should move independently, which implies that

$$\langle \Delta^2(t)\rangle = 2\langle Y^2(t)\rangle = G_\Delta^{\mathrm{N}} \epsilon t^3, \tag{4.9}$$

where $G_\Delta^{\mathrm{N}} = 2G_Y = 4\pi C^{\mathrm{L}}$.

Kraichnan (1966) derived a value for $G_\Delta = 2.42$ on the basis of a Lagrangian history direct interaction (LHDI) calculation which involves introducing an instantaneous eddy diffusivity. Lundgren (1981) used a modified LHDI calculation to obtain $G_\Delta = 3.0$, while Larchevêque & Lesieur's (1981) EDQNM closure approximation yields $G_\Delta = 3.5$. Thomson (1990) has developed a two-particle stochastic random flight model from which $G_\Delta = 2.0$.

4.2.2. *The dependence on initial separation and the inertial range*

In each of seven different ensembles of flow fields using KSIM, the value of $\langle \Delta^2(t)\rangle$ was computed for a range of initial separations. Each ensemble was characterized by a particular range of inertial subrange (see table 3). Five different initial separations were tested in each ensemble: $\Delta_0/\eta = 0.025$, 0.05, 0.1, 0.2 and 0.4, where η is the Kolmogorov scale of the particular flow ($\eta = 2\pi/k_\eta$).

We have varied the number of modes (N_k and P_ω) for those simulations where the inertial subrange was less than or equal to 2-decades (100). We found that the minimum number of modes needed for consistent results for the mean-square separation $\langle \Delta^2 \rangle$ varies approximately linearly with the inertial subrange, starting with 30 modes for $k_\eta = 10$. This determined the number of modes for those simulations with inertial ranges greater than 2-decades (see table 3).

In figure 12, we have plotted the results for the case $k_\eta = 200$ in the form of log

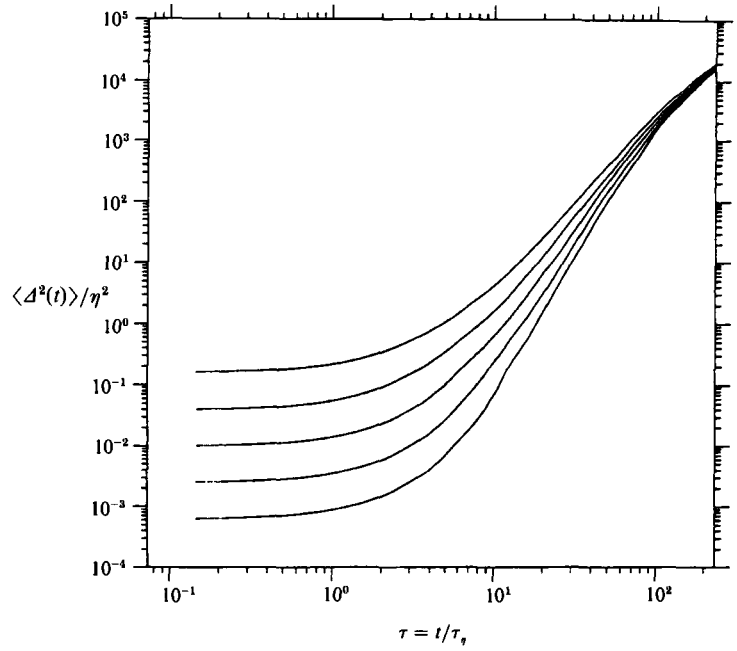

FIGURE 12. Mean-square separation $\langle \Delta^2(t)\rangle/\eta^2$ plotted against time t/τ_η, for an inertial subrange $1 \leqslant k \leqslant k_\eta = 200$ and for five values of the initial separation: $\Delta_0/\eta =$ (1) 0.025, (2) 0.05, (3) 0.1, (4) 0.2, (5) 0.4, where $\eta = 2\pi/k_\eta$ is the Kolmogorov scale; $\tau_\eta = \epsilon^{-\frac{1}{3}}k_\eta^{-\frac{2}{3}}$ is the Kolmogorov time microscale.

$\{\langle \Delta^2(t)\rangle/\eta^2\}$ against $\log\{t/\tau_\eta\}$, where τ_η is the Kolmogorov time microscale ($= \epsilon^{-\frac{1}{3}}k_\eta^{-\frac{2}{3}}$). Results for other values of k_η are similar. At small times $\langle \Delta^2(t)\rangle$ clearly depends upon Δ_0, but as time increases the curves tends towards the same line. This is because the motion at scales less than the Kolmogorov lengthscale is effectively a uniform straining and it takes a finite time, $t_\eta (\sim \epsilon^{-\frac{1}{3}}k_\eta^{-\frac{2}{3}} \ln\{\eta/\Delta_0\})$, for the particle separation to reach the Kolmogorov scale. When the results are replotted as $\log\{(\langle \Delta^2(t)\rangle - \eta^2)/\eta^2\}$ against a false origin in time ($t_s = t - t_\eta$) all the curves lie on the same line, to within 15%. (The subtraction of η^2 rather than Δ_0^2 is to allow a direct comparison with $\langle Y^2\rangle$. In the inertial subrange where $\langle \Delta^2(t)\rangle \gg \eta^2$, this is not an important difference.)

Then $\langle \Delta^2\rangle$ was computed for seven different sizes of inertial subrange (see table 3) and the results for the case when $\Delta_0/\eta = 0.4$ are shown in figure 13 plotted in the form $\log\{(\langle \Delta^2(t_s)\rangle - \eta^2)/\eta^2\}$ against $\log\{t_s\}$. The slopes of the lines increase as k_η/k_c increases, and the coefficient G_Δ decreases; the values are given in table 3. In the inertial subrange the relationship between $\langle \Delta^2(t_s)\rangle$ and t_s must be of the form

$$\langle \Delta^2(t_s)\rangle = Ct_s^\gamma, \tag{4.10}$$

where γ and C are both functions of k_η/k_c. The computed values of these coefficients have been plotted against k_η/k_c in figure 14. These graphs show that as the size of the inertial subrange increases, γ tends to 3, as observed by Richardson (1926) and predicted by Obukhov. The value of C tends to 0.05. Substituting this into (4.7) (which was derived by Obukhov 1941 assuming an infinite inertial subrange) we obtain $G_\Delta \to 0.1$, since $\epsilon \to 0.544$ as $k_\eta/k_c \to \infty$.

Examining the difference between the structure function D_{11} and its asymptotic

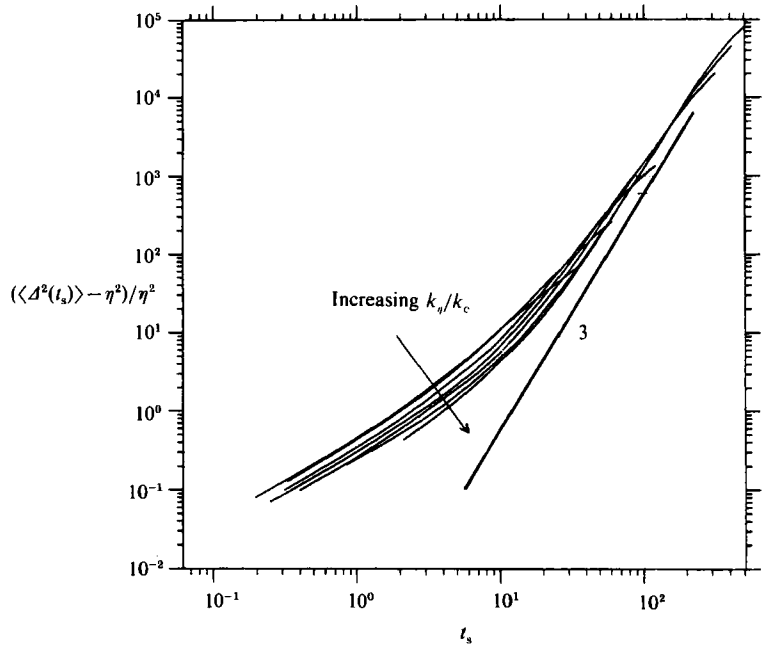

FIGURE 13. Comparison of $(\langle \Delta^2(t_s)\rangle - \eta^2)/\eta^2$ against *false origins* in time $t_s = [t - t_\eta(\Delta_0)]/\tau_\eta$, for seven different ranges of the inertial subrange: $1 \leqslant k \leqslant k_\eta = 10, 20, 50, 100, 200, 300, 400$. In each case, we have $\Delta_0/\eta = 0.4$. The slopes of the curves tend to 1.6, 1.9, 2.3, 2.6, 2.78, 2.95 and 2.97 respectively. A line of slope 3 is shown for comparison.

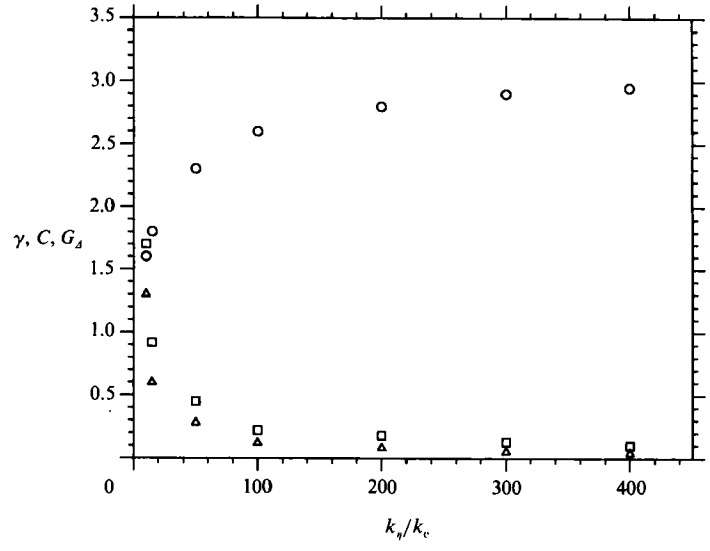

FIGURE 14. Plot of the constants γ, C and G_Δ, where $C = G_\Delta \epsilon$ and $\langle \Delta^2(t_s)\rangle = C t_s^\gamma$, against different sizes of the inertial subrange k_η/k_c: ○, $\gamma(\rightarrow 3$ as k_η/k_c increases, as predicted from Kolmogorov's theory); △, C; □, $G_\Delta(\rightarrow 0.1$ as k_η/k_c increases).

form, (2.20), shows that $\Delta^2(t)$ only reaches its asymptotic form in the inertial range when $k_\eta/k_c \gg 100$. We note that only in large-scale geophysical or astrophysical turbulence is it likely that the Reynolds number and the ratio k_η/k_c will be large enough for the Richardson–Obukhov separation to be observed. For example, in the

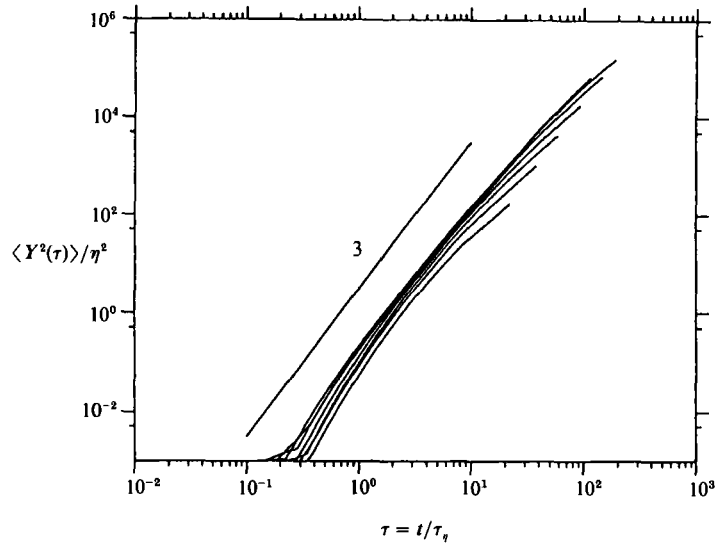

FIGURE 15. The mean square difference $\langle Y^2(\tau)\rangle/\eta^2$ plotted against time $\tau = t/\tau_\eta$, for seven different ranges of the inertial subrange as in figure 13. A line of slope 3 is drawn for comparison.

atmosphere, in strong convection, $k_\eta/k_c \sim 10^5$, but in laboratory turbulence it is impossible to obtain a large enough ratio of k_η/k_c.

4.2.3. *The difference statistics*

We have computed the difference statistics, i.e. the displacement of a single particle relative to its initial trajectory $Y(t)$, for the same ranges of inertial subrange as in the previous sections (table 3). The results are plotted in figure 15 in the form $\log\{\langle Y^2(t)\rangle/\eta^2\}$ against $\log\{t/\tau_\eta\}$, and a line of slope 3 is plotted for comparison. The computed values of G_Y and γ_y (where $\langle Y^2\rangle = G_Y \epsilon t^{\gamma_y}$) as a function of k_η/k_c are plotted in figure 16. $\gamma_y \to 3.0$ and $G_Y \to 5.0$ approximately as $k_\eta/k_c \to \infty$ (although the rate of convergence of γ_y to a limit is slow for $k_\eta/k_c \gtrsim 200$). This estimate is close to the theoretical value of $2\pi C^L = 5.11$ based on $C^L = 0.81$ from (4.8*c*). Since this relation between G_Y and C^L is an exact result, the present simulation results for G_Y are a satisfactory consistency check on KSIM. But this result and the slow convergence of γ_y shows that a large inertial range would be needed to produce a noticeable t^3-regime in $\langle Y^2\rangle$; at least $k_\eta/k_c > 10^3$.

We can now compare the direct two-particle results with Novikov's prediction; we estimate from our computations that in the limit $k_\eta/k_c \to \infty, \mathscr{R}_G = 2G_Y/G_\Delta \approx 100$.

4.2.4. *'Structural' dispersion*

The value of G_Δ can be predicted by a simple calculation that contains the essence of these models (except Novikov's). It is assumed that the particles move apart in a straining motion so that $\mathrm{d}\Delta/\mathrm{d}t$ is approximately equal to the velocity difference at a distance Δ. Then from (2.21), in one direction $\mathrm{d}\Delta/\mathrm{d}t \approx 1.6\epsilon^{\frac{1}{3}}\Delta^{\frac{1}{3}}$. Assuming Δ increases on average in only two directions, we estimate

$$\langle \Delta^2\rangle \approx 3\epsilon t^3, \tag{4.11}$$

which is close to the results of statistical models described in §4.2.1.

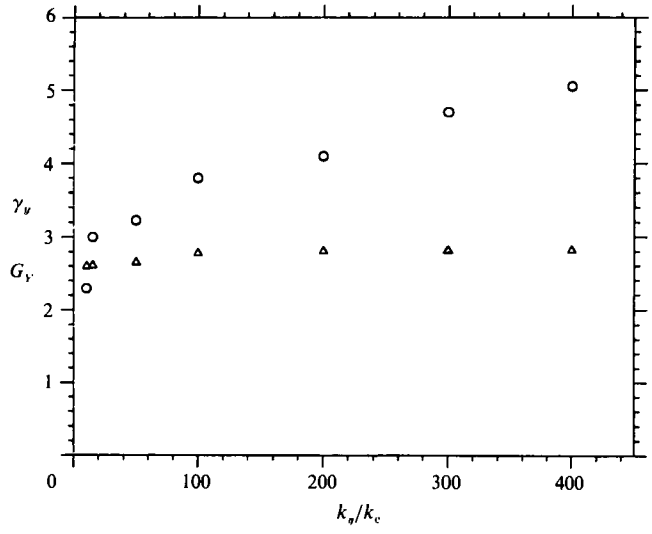

FIGURE 16. The exponent γ_v (○), where $\langle Y^2(t)\rangle = Ct^{\gamma_v}$ and the constant G_Y (△), where $\langle Y^2(t)\rangle = G_Y \epsilon t^{\gamma_v}$, plotted against the different size of the inertial subranges k_η/k_c; $G_y \to 5.0$ approximately as k_η/k_c increases, as predicted by Novikov (1963).

This model (and the stochastic models) implicitly assumes that $\mathrm{d}\Delta/\mathrm{d}t$ is parallel to Δ. However, this can only be (approximately) correct in straining regions – it is certainly not correct in vortical regions, where $\boldsymbol{\omega}$ is the local vorticity and $\mathrm{d}\Delta/\mathrm{d}t \propto (\Delta \wedge \boldsymbol{\omega})$. Hence, $\langle \Delta \cdot \mathrm{d}\Delta/\mathrm{d}t\rangle$ is effectively proportional to the fraction of time f_c that a particle spends in the convergence–divergence regions where the strain rate is greater than the vorticity. Therefore (4.11) should be modified to

$$\mathrm{d}\Delta_1/\mathrm{d}t \approx f_c(1.6\epsilon^{\frac{1}{3}}\Delta^{\frac{1}{3}}), \quad \text{whence} \quad \langle \Delta^2\rangle \sim 3f_c^3\epsilon t^3. \tag{4.12}$$

But, since all regions of the flow contribute to the increases in Y, not just the straining regions, $\langle Y^2\rangle$ is independent of f_c and $2\langle Y^2\rangle \sim 10\epsilon t^3$ from (4.8c). Therefore

$$\mathscr{R}_G = 2\langle Y^2\rangle/\langle \Delta^2\rangle \approx O(3f_c^{-3}). \tag{4.13}$$

In order that particles can separate in straining motion at a rate proportional to $D_{11}(\Delta)$, it is necessary that $\mathrm{II} \gtrsim \mathrm{II}_{\mathrm{rms}}$. (Note that if $0 < \mathrm{II} < \mathrm{II}_{\mathrm{rms}}$, the particles do not necessarily separate.) Therefore the proportion (f_c) of the time that a particle spends in regions where $\mathrm{II} \gtrsim \mathrm{II}_{\mathrm{rms}}$ is less than half. In simulations by Malik (1991) $f_c \approx 0.3$. Hence from (4.12) $\langle \Delta^2\rangle \approx 0.1\epsilon t^3$, and $\mathscr{R}_G \approx 110$. These estimates are very close to the results of the simulation!

In all the statistical models, some assumptions were made about the relevant statistics of the flow field for dispersing the particles and their relation to the Eulerian statistics of turbulence, but they could not account for actual forms of three-dimensional random velocity fields.

A simple way to visualize this result is to consider a fluid element released in a vortex region, with its 'imaginary' partner (figure 17). The real particle is advected by the flow around the vortex or other eddy structure, while the 'imaginary' particle will continue to move in a straight line. Soon after release, they may even travel in opposite directions, at which point the displacement will increase rapidly. However, if a second real particle is released close to the first one, it will in general follow a

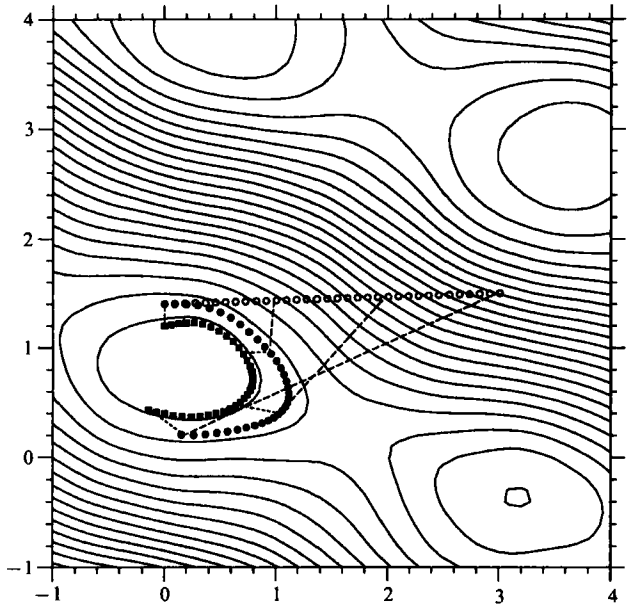

FIGURE 17. Illustrating 'structural' diffusion. Streamlines of a stationary two-dimensional flow are shown, but the phenomenon generalizes immediately for unsteady three-dimensional flows. A real particle (filled circle) and an imaginary particle (open circle) have the same initial conditions, but the latter continues on its initial projection. A second real particle (filled square) is released close to the first. The separation between the real particles remain small (dotted line) as they are advected by the local vortex, but the distance between a real particle and its imaginary partner (dashed line) increases rapidly: $\langle Y^2 \rangle \gg \langle \Delta^2 \rangle$.

k_c/L	k_η/L	ϵ	u_1^2/u_s^2	$u_1^3 k_c/\epsilon$	C_p
1.5	50.0	0.6377	0.3060	0.266	0.407
3.0	50.0	0.7582	0.9690	1.365	0.429
5.0	50.0	1.0660	1.3810	2.072	0.457
7.0	50.0	0.8045	2.8628	5.550	0.501
5.0	25.0	0.8638	2.2725	3.347	0.376
5.0	100.0	1.0365	1.2053	1.946	0.465

TABLE 4. Coefficients of the variance of pressure fluctuations for different simulations

trajectory that is close to the first particle, and the displacement between them, Δ, remains much smaller than the displacement from the imaginary particle. Thus $\langle Y^2 \rangle \gg \Delta^2$ in these vortical regions. The pair remain close together until they enter a region of high local strain where streamlines diverge; they will then tend to separate. These kinds of trajectories of pairs of fluid elements were observed by Wilkins (1958) in atmospheric turbulence.

Perhaps one might qualify Richardson's (1926, p. 711) description of relative diffusion by saying that it occurs intermittently depending on how the particles are placed in relation to the form and lengthscale of the local eddy motion; in turbulence jargon it is an 'intermittent inverse cascade process'. This result shows how the statistical theory can be improved by considering the structure of the flow.

4.2.5. *Note on simulation*

There are several possible sources of error in this estimate of G_Δ. As mentioned in §4.2.4, as the extent of the inertial range (k_η/k_c) is increased the slope of the Lagrangian spectrum increases and changes to $-\frac{5}{3}$. This effect of large inertial-range eddies advecting particles past small eddies increases the mean-square velocity of the particles $(\mathrm{d}\Delta/\mathrm{d}t)^2$, but it also reduces the timescale of $\mathrm{d}\Delta/\mathrm{d}t$. It seems likely that the former effect dominates and therefore G_Δ is, for this reason, perhaps too large. Another error, whose effect on Δ^2 is uncertain, is the contribution of vortex stretching near stagnation regions, which is not modelled by KS. But a study of one-particle diffusion in a stagnation region shows that this is a small effect compared to that of the large-scale diverging/converging motions which are simulated by the model (Hunt 1985).

5. Pressure field

5.1. *The mean-square pressure fluctuation*

Using KSSM to compute the fluctuating pressure field, as outlined in §2.7, we have evaluated $\langle p^2\rangle$ by computing the pressure at 4900 different points at one instant in time and then taking the ensemble average. We have tested the sensitivity of the constant $C_p = \langle p^2\rangle/\rho^2(\langle u^2\rangle)^2$ by varying both the separation between the large- and small-scale fields (k_c) and the cutoff wavenumber k_η. The results are shown in table 4. The simulations all suggest that for high-Reynolds-number turbulence for $k_\eta/L \geqslant 50.0$, $0.4 < C_P < 0.5$. For high-Reynolds-number turbulence there is good agreement between this simulation and previous theoretical models of Hinze (1975), who predicted $C_p = 0.15$ and George, Beuther & Arndt (1984) who obtained 0.42.

5.2. *Pressure spectra*

In previous theoretical investigations by directly Fourier transforming the integral solution to the Poisson equation for a homogeneous constant-mean-shear flow (e.g. George *et al.* 1984) it has been suggested that pressure fluctuations at small scales have been caused by the motions of eddies on that scale, and not by interaction between small scales and large scales, which led to the prediction for the energy spectrum

$$\left.\begin{aligned} E_{pp}(k) &= \alpha_{kp}\epsilon^{\frac{4}{3}}k^{-\frac{7}{3}} \quad \text{for} \quad k_0 \ll k \ll \eta^{-1}, \\ E_{pp_1}(k_1) &= \alpha_{kp_1}\epsilon^{\frac{4}{3}}k_1^{-\frac{7}{3}} \quad \text{for} \quad k_0 \ll k_1 \ll \eta^{-1}, \end{aligned}\right\} \tag{5.1}$$

where the coefficients for three- and one-dimensional pressure spectra, α_{kp} and α_{kp_1} are universal constants analogous to the Kolmogorov constant for the velocity spectrum (Monin & Yaglom 1975). Batchelor (1951) calculated the value of α_{kp} by using the zero-fourth-cumulant hypothesis for the velocity and assuming a simple transition function $B_{11}(y) = (\nu\epsilon)^{-\frac{1}{2}}D_{11}(\eta y)$ of the form

$$B_{11}(y) = \tfrac{1}{15}y^2[1+(15C)^{-\frac{3}{2}}y^2]^{-\frac{2}{3}},$$

which is valid for both $y \ll 1$ and $y \gg 1$, for the velocity structure function D_{11}. According to his results, $\alpha_{kp} \approx 0.354C^{\frac{3}{2}}$, and from experiments $C = 2$, so $\alpha_{kp_1} \approx 1$.

The one-dimensional pressure spectrum $E_{pp}(k_1)$ was computed from the random pressure field (figure 18). The graph shows a 'slope' of $-\frac{7}{3}$ as predicted by the inertial

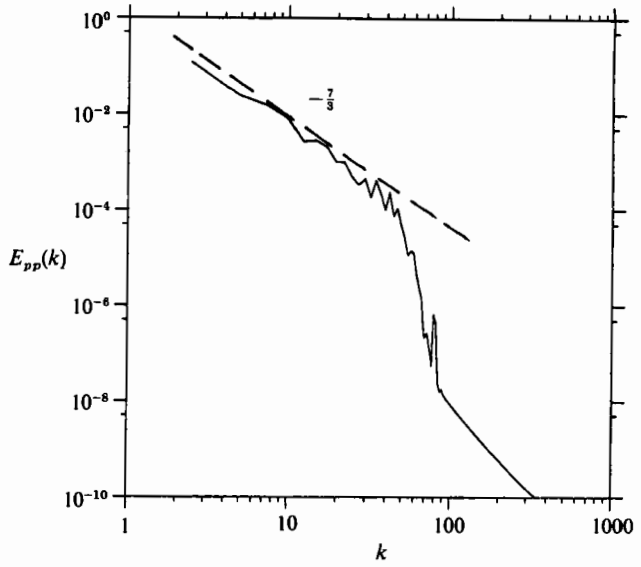

FIGURE 18. Average pressure spectrum in wavenumber space $E_{pp}(k)\,(=\alpha_{kp}\epsilon^{\frac{4}{3}}k^{-\frac{7}{3}})$ with a $-\frac{7}{3}$ slope. This is consistent with the results of George *et al.* (1984).

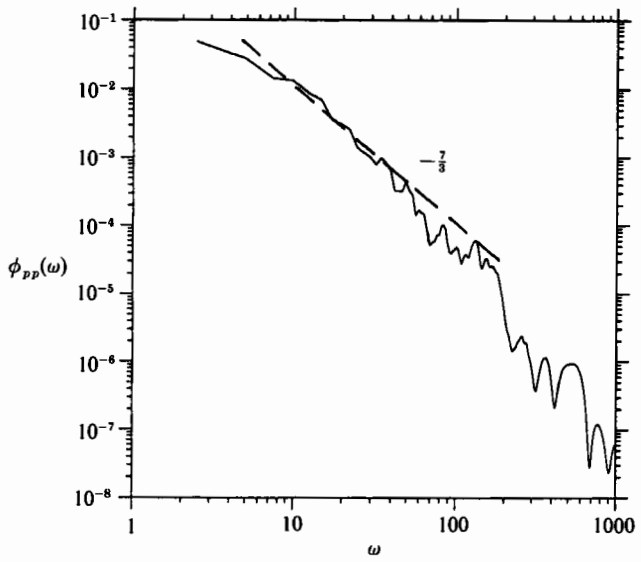

FIGURE 19. Average pressure spectrum in frequency space $\phi_{pp}(\omega)\,(\propto (a_p\epsilon U_0)^{\frac{4}{3}}(\omega)^{-\frac{7}{3}})$ with a $-\frac{7}{3}$ slope. This result was also obtained by Chase (1970).

range theory (5.1). The coefficient α_{kp_1} obtained from figure 18, is given by $\alpha_{kp_1}\epsilon^{\frac{4}{3}} = 1.0$, so $\alpha_{kp_1} = 0.92$. This is close to the value $\alpha_{kp_1} \approx 1.0$ obtained from Batchelor's (1951) result for $\alpha_{kp} = 7\alpha_{kp_1}/3 \approx 2.6$.

Chase (1970) and Hunt *et al.* (1987) suggested that, as the large-scale eddies advect the small eddies, they also advect the small-scale pressure fluctuations. By analogy with the velocity spectrum $\mathscr{E}(k,\omega)$, (2.26), the k–ω power spectrum of pressure fluctuations is expected to have the form

$$\mathscr{E}_{pp}(k,\omega) = E_{pp}(k)\exp[-\tfrac{1}{2}\omega^2/(a_p kU_0)^2]/((2\pi)^{\frac{1}{2}}a_p kU_0). \tag{5.2}$$

As in (2.28), $\phi_{pp}(\omega) = \int \mathscr{E}_{pp}(k,\omega)\,\mathrm{d}k$ and we obtain

$$\phi_{pp}(\omega) = C_p(a_p \epsilon U_0)^{\frac{4}{3}}\omega^{-\frac{7}{3}}, \tag{5.3}$$

where $C_p = 4\alpha_{kp}\Gamma(\frac{7}{6})/2^{\frac{1}{3}}\pi^{\frac{1}{2}}$. Taking the high-Reynolds-number value of $a_p = 1.0$, $C_p = 0.9(a_p \epsilon U_0)^{\frac{4}{3}} = 0.2$.

The pressure frequency spectrum $\phi_{pp}(\omega)$ obtained from KS is presented in figure 19 and follows the $\omega^{-\frac{7}{3}}$ law of (5.3), but the $-\frac{7}{3}$ law extends over only one decade. But the constant of proportionality of 1.14 in the simulation does not agree with the value of 0.2 predicted from the asymptotic theory, for an infinitely large ($-\frac{5}{3}$) range. We do not have a satisfactory explanation for this discrepancy.

6. Conclusions

We have presented here a simulation of an unsteady random velocity field, whose statistics are adjusted to agree with the experimentally measured values of two-point space–time Eulerian and Lagrangian statistics of homogeneous turbulence. This kinematic simulation should be useful in many studies which require such flow fields, and where there is no model for the small scale at present – it is a kind of 'small-eddy simulation' that might complement large-eddy simulation. The simulation is not equivalent to that of a turbulent flow in two important respects: the vortical regions are not sufficiently elongated and the higher-order statistics are too closely Gaussian. The reason is that the simulation does not represent the dynamical processes in turbulence, which for example stretch vortices and affect higher-order statistics by making the turbulence intermittent. But the fact that the Lagrangian and pressure statistics agree with measurements suggests that these detailed aspects of the flow are not so important when modelling many aspects of dispersion, combustion, two-phase flow, etc.

Following the work of Lee *et al.* (1990) and Turfus & Hunt (1986), it is possible to extend this simulation to include other effects such as shear and the presence of the boundaries. Calculations involving the dynamical interactions between eddies on different scales or dynamics in local regions of the flow may be one way forward to examine the errors in the flow structure in kinematic simulation caused by ignoring these interactions. In short there may be several alternative strategies for simulating turbulent velocity fields other than straightforward computation of the dynamical equations.

We are grateful to our DAMTP colleagues I. T. Drummond, R. R. Horgan and C. Turfus for stimulating this work. J. C. R. H. is grateful for conversations with M. Lee, R. Metcalfe, P. Moin and A. Wray which led to some of the ideas presented here. J. C. H. F. gratefully acknowledges financial support from Peterhouse and the use of computing resources at UKAEA Harwell. N. A. M. gratefully acknowledges financial support from SERC and CEGB and the use of computing resources at RAL via an SERC grant, and R. J. P. was supported by DTI Warren Spring Laboratory and the Wolfson Foundation.

Appendix A

Consider the small-scale velocity field represented in complex form by

$$u_i(\boldsymbol{x},t) = \sum_{n=-N}^{N} A_i^{(n)} \exp\{\mathrm{i}[\kappa_j^{(n)} X_j - \omega_n' t]\}, \tag{A 1}$$

where $$A_i^{(n)} = \epsilon_{ijk}(a_k^{(n)} \hat{\kappa}_j^{(n)} - b_k^{(n)} \hat{\kappa}_j^{(n)}),$$

and the Fourier coefficients $a_i^{(n)}$ are independent of time. Let $u = u_s$ and $U = u_l$; then by expanding about the particle position $\boldsymbol{x}^0$, X_j can be expressed in term of gradients of the large-scale sweeping motion,

$$\begin{aligned} X_j &= x_j + \int_0^t U_j(\boldsymbol{x}(t'),t')\,\mathrm{d}t' \\ &= x_j + \int_0^t U_j(\boldsymbol{x}^0,t')\,\mathrm{d}t' - \int_0^t \frac{\partial U_j}{\partial x_k}(\boldsymbol{x}^0,t')\,[x_k(t') - x_k^0(t')]\,\mathrm{d}t' + O\left(\frac{\partial^2 U}{\partial x^2}\right). \end{aligned} \tag{A 2}$$

Then $$\frac{\partial X_j}{\partial x_i} = \delta_{ij} - \int_0^t \frac{\partial U_j}{\partial x_k}(\boldsymbol{x}^0,t')\frac{\partial x_k}{\partial x_i}(t')\,\mathrm{d}t' + \ldots.$$

Let $(\partial x_k/\partial x_i)(t') = \xi_{ki}(t')$, then we have $\partial \xi_{ki}/\partial \tau = (\partial U_k/\partial x_i)(\boldsymbol{x}(\tau),\tau)$.

Note that for conservation of wave fronts (Townsend 1976), the wavevector must satisfy the differential equation

$$\frac{\partial k_j}{\partial t} + U_j \frac{\partial k_j}{\partial x_i} + k_j \frac{\partial U_j}{\partial x_i} = 0.$$

The above equation is evaluated at the particle position $(\boldsymbol{x}^0, t)$.

Thus the wavevector $\boldsymbol{\kappa}$ of the small-scale velocity field varies in time and slowly in space. Taking the divergence of u_i in (A 1), together with (A 2), we obtain

$$\begin{aligned} \frac{\partial u_i}{\partial x_i} = \sum_n \mathrm{i}\Bigg\{ & A_i^{(n)} k_i^{(n)}(t) + A_i^{(n)} k_j^{(n)} \int_0^t \frac{\partial U_j}{\partial x_k}(\boldsymbol{x}^0,t')\frac{\partial x_k}{\partial x_i}(t')\,\mathrm{d}t' + \ldots \\ & + A_i^{(n)} X_j \frac{\partial k_j}{\partial x_i}\Bigg\} \exp\{\mathrm{i}[k_j^{(n)} X_j - \omega' t]\}. \end{aligned} \tag{A 3}$$

But $$k_i(t) = k_i(t=0) + \int_0^t \frac{\partial k_i}{\partial t}\,\mathrm{d}t.$$

Substituting this into (A 3), and using the condition of incompressibility, $\partial u_i/\partial x_i = 0$, requires that for each wavenumber mode we must have (dropping the superscript n)

$$A_i k_i(t=0) + A_i\left[\int_0^t \frac{\partial k_i}{\partial t'} + k_j\left(\frac{\partial U_j}{\partial x_k}(\boldsymbol{x}^0,t')\frac{\partial x_k}{\partial x_i}(t') + \ldots\right)\mathrm{d}t'\right] + A_i x_j \frac{\partial k_j}{\partial x_i} = 0. \tag{A 4}$$

Then continuity may be satisfied by satisfying three additional conditions namely:

(i) $A_i k_i(t=0) = 0$ (this is satisfied by continuity);

(ii) $k_j(\boldsymbol{x}) =$ constant (over any region of effectively uniform straining);

(iii) Let k_j vary with time such that

$$\frac{\partial k_i}{\partial t} = -k_j \frac{\partial U_j}{\partial x_k}(\boldsymbol{x}^0,t')\frac{\partial x_k}{\partial x_i}(t'). \tag{A 5}$$

Appendix B

It follows from (2.4) (also see Fung 1990) that the change in $\partial \boldsymbol{u}_l/\partial t$ associated with changing k_c (or N_c) is of order

$$|(\boldsymbol{a}_{N_c-1} \wedge \hat{\boldsymbol{\kappa}}_{N_c-1}) \cdot \partial \boldsymbol{\zeta}_{N_c-1}/\partial t| \sim |(\boldsymbol{a}_{N_c-1} \wedge \hat{\boldsymbol{\kappa}}_{N_c-1}) \cdot \boldsymbol{W}_{N_c-1}|. \tag{B 1}$$

But the change in $|\partial \boldsymbol{u}_s/\partial t|$ is of order

$$|(a_{N_c} \wedge \hat{\boldsymbol{\kappa}}_{N_c}) \cdot \partial \boldsymbol{x}_L/\partial t - \omega_n'| \sim |(\boldsymbol{a}_{N_c} \wedge \hat{\boldsymbol{\kappa}}_{N_c} \cdot \boldsymbol{u}_l - \omega_n'|). \tag{B 2}$$

Since $|\boldsymbol{W}_{N_c-1}| < |\boldsymbol{u}_l|$, it follows that as k_c decreases, $|\partial \boldsymbol{u}/\partial t| \sim |\boldsymbol{a}_{N_c} \wedge \hat{\boldsymbol{\kappa}}_{N_c} \cdot \boldsymbol{u}_l - \omega_n'|$, and as k_c increases, $|\partial \boldsymbol{u}/\partial t| \sim |(\boldsymbol{a}_{N_c-1} \wedge \hat{\boldsymbol{\kappa}}_{N_c-1}) \cdot \boldsymbol{W}_{N_c-1}|$. Since $|\boldsymbol{W}_{N_c}| > |\boldsymbol{u}_l|$, it follows that as k_c decreases, $\partial u/\partial t$ decreases and R^E increases. For a small value of k_c, $R_{11}^E(\tau)$ always exceeds $R_{11}^L(\tau)$, and there is no 'crossover' value of τ of which $R_{11}^E(\tau) = R_{11}^L(\tau)$.

Appendix C

To simulate the small-scale eddies as well as the large-scale ones, consider a set of small eddies moved by a random large-scale velocity $\boldsymbol{u}_l(\boldsymbol{x}, t)$; then from (2.7)

$$\boldsymbol{u}_s(\boldsymbol{x}, t) = \sum_{n=-N}^{N} \boldsymbol{a}_n \exp\left\{ i\left[\boldsymbol{\kappa}_n \cdot \left(\boldsymbol{x}(t) - \int_0^t \boldsymbol{u}_l(\boldsymbol{x}(t'), t')\, dt' \right) + \omega_n' t \right] \right\}, \tag{C 1}$$

where ω_n' is the frequency in the advected frame, and is determined from the spectra (or structure function) which must be correct in a frame moving with $\boldsymbol{u}_l$.

Since the local fluid velocity $\boldsymbol{u}(\boldsymbol{x}, t)$ is mainly determined by the large eddies, it is relatively constant over the space–time region of $r \ll L$ and $\tau \ll L/|\boldsymbol{u}_l|$ (since $\boldsymbol{u}_l(\boldsymbol{x}, t)$ changes slowly with time). Therefore, over short times $\tau_L \ll \tau \ll T_L$, where $\tau_L \sim Re^{-\frac{1}{4}} T_L$, the Eulerian–Lagrangian autocorrelation function of $\boldsymbol{u}_s(\boldsymbol{x}, t)$ in a frame moving with the large-scale eddies has a form

$$R^{EL}(\tau) = \langle \boldsymbol{u}_s(\boldsymbol{X}(t), t) \cdot \boldsymbol{u}_s(\boldsymbol{X}(t+\tau), t+\tau) \rangle^{EL}.$$

By translational invariance this becomes

$$R^{EL}(\tau) = \langle \boldsymbol{u}_s(0, t) \cdot \boldsymbol{u}_s(\boldsymbol{X}(t+\tau) - \boldsymbol{X}(t), t+\tau) \rangle^{EL},$$

where $\boldsymbol{X}(t)$ is defined as in (2.8), i.e. $\boldsymbol{X} = \boldsymbol{x} - \boldsymbol{x}_L$, where $\boldsymbol{x}(t)$ is the *particle* position at time t. Hence

$$\begin{aligned} R^{EL}(\tau) &= \left\langle \boldsymbol{u}_s(0, t) \cdot \boldsymbol{u}_s\left(\int_0^{t+\tau} \boldsymbol{u}_l(\boldsymbol{x}(t', \boldsymbol{x}(t+\tau), t')\, dt' - \int_0^t \boldsymbol{u}_l(\boldsymbol{x}(t', \boldsymbol{x}(t), t')\, dt' \right) \right\rangle \\ &\approx \sum_{n=-N}^{N} \sum_{m=-N}^{N} \langle \boldsymbol{a}_n \cdot \boldsymbol{a}_m^* \rangle e^{i\omega_n' \tau} \\ &= 2 \sum_{n=N_c}^{N_\eta} \langle |\boldsymbol{a}_n|^2 \rangle e^{i\omega_n' \tau}, \end{aligned} \tag{C 2}$$

we have used the condition that the modes are independent of each other, i.e. $\langle \boldsymbol{a}_n \cdot \boldsymbol{a}_m^* \rangle = \delta_{mn}$. This represents an average over the motion of scale small compared with L only. Let

$$\omega_n' = \lambda \epsilon^{\frac{1}{3}} k_n^{\frac{2}{3}}, \tag{C 3}$$

where λ is a constant of proportion and of order unity. This is the 'natural' eddy

timescale introduced by Edwards (1964) – see Leslie (1973). We will show that such choice of ω_n' is consistent with the Eulerian–Lagrangian result of $R_{11}^{\mathrm{EL}}(\tau) = \langle u_1^2\rangle - 2\pi C^{\mathrm{EL}}\epsilon\tau$, where ϵ is the dissipation of turbulent kinetic energy per unit mass and C^{EL} is a constant.

By letting $k_n = nk_{\mathrm{c}}\,\omega_n' = \lambda\epsilon^{\frac{1}{3}}k_{\mathrm{c}}^{\frac{2}{3}}n^{\frac{2}{3}}$, we have

$$R_{11}^{\mathrm{EL}}(\tau) = \tfrac{2}{3}A\sum_{n=N_{\mathrm{c}}}^{N_\eta} n^{-\frac{5}{3}}\exp(\mathrm{i}n^{\frac{2}{3}}p), \tag{C 4}$$

where $p = \lambda\epsilon^{\frac{1}{3}}k_{\mathrm{c}}^{\frac{2}{3}}\tau$ and $A = \alpha_k\,\epsilon^{\frac{2}{3}}k_{\mathrm{c}}^{-\frac{2}{3}}$. To compute the sum in (C 4), we assume n/n_{c} is large so that the finite sum reduces to an integral, i.e.

$$\begin{aligned} R_{11}^{\mathrm{EL}}(\tau) &= \tfrac{2}{3}A\int_{n_{\mathrm{c}}}^{n_\eta} n^{-\frac{5}{3}}\mathrm{e}^{\mathrm{i}n^{\frac{2}{3}}p}\,\mathrm{d}n = Ap\int_{q_0-pn_{\mathrm{c}}^{\frac{2}{3}}}^{q_\eta-pn_\eta^{\frac{2}{3}}} q^{-2}\mathrm{e}^{\mathrm{i}q}\,\mathrm{d}q \\ &\approx \langle u_{\mathrm{s}}^2\rangle - \tfrac{1}{2}\pi\alpha_k\lambda\epsilon\tau + \alpha_k\lambda^2\epsilon^{\frac{4}{3}}k_{\mathrm{c}}^{\frac{2}{3}}\tau^2 - 2\alpha_k\epsilon^{\frac{2}{3}}k_\eta^{-\frac{2}{3}}\cos(\omega_\eta\tau). \end{aligned}$$

For an infinite inertial range $k_{\mathrm{c}}\to 0$ and $k_\eta\to\infty$, R_{11}^{EL} reduces to

$$R_{11}^{\mathrm{EL}} \approx \langle u_{\mathrm{s}}^2\rangle - \pi C^{\mathrm{EL}}\epsilon\tau, \tag{C 5}$$

where $q_{\mathrm{c}} = pn_{\mathrm{c}}^{\frac{2}{3}}$ and $C^{\mathrm{EL}} \approx \frac{1}{2}\alpha_k\lambda$.

If we define $\boldsymbol{u}_{\mathrm{s}}(\boldsymbol{x},t)$ as scales less than, say, $10t^{\frac{3}{2}}\epsilon^{\frac{1}{2}}$, and from the similarity law, $\epsilon \sim u_{\mathrm{s}}^3/l_{\mathrm{s}} \sim u_{\mathrm{s}}^2/\tau$, then the displacement due to the small-scale eddies in time τ is

$$\boldsymbol{x}_{\mathrm{s}} = \int_0^\tau \boldsymbol{u}_{\mathrm{s}}(\boldsymbol{x},t')\,\mathrm{d}t' \sim O(\tau\epsilon^{\frac{1}{3}}l_{\mathrm{s}}^{\frac{1}{3}}) \sim O(\tau^{\frac{3}{4}}\epsilon^{\frac{1}{2}}). \tag{C 6}$$

Now consider the Lagrangian velocity correlation function of $\boldsymbol{u}_{\mathrm{s}}(\boldsymbol{x},t)$, along the fluid element trajectories, i.e.

$$\begin{aligned} R^{\mathrm{L}}(\tau) &= \langle \boldsymbol{u}_{\mathrm{s}}(t)\cdot\boldsymbol{u}_{\mathrm{s}}(t+\tau)\rangle^{\mathrm{L}} \\ &= \langle \boldsymbol{u}_{\mathrm{s}}(\boldsymbol{x},t)\cdot\boldsymbol{u}_{\mathrm{s}}(\boldsymbol{x}+\boldsymbol{x}_{\mathrm{L}}+\boldsymbol{x}_{\mathrm{s}},t+\tau)\rangle^{\mathrm{E}} \\ &= R^{\mathrm{EL}}(\tau) + \Delta R^{\mathrm{L}}, \end{aligned} \tag{C 7}$$

where ΔR^{L} is the difference in the correlation between A^{L} and A, and A^{EL} and A (the dispersion due to small-scale correlation), i.e.

$$\Delta R^{\mathrm{L}} = \langle \boldsymbol{u}_{\mathrm{s}}(\boldsymbol{x},t)\cdot\boldsymbol{u}_{\mathrm{s}}(\boldsymbol{x}+\boldsymbol{x}_{\mathrm{L}}+\boldsymbol{x}_{\mathrm{s}},t+\tau)\rangle - \langle \boldsymbol{u}_{\mathrm{s}}(\boldsymbol{x},t)\cdot\boldsymbol{u}_{\mathrm{s}}(\boldsymbol{x}+\boldsymbol{x}_{\mathrm{L}},t+\tau)\rangle.$$

Assuming $\quad \Delta R^{\mathrm{L}} \leqslant |\langle \boldsymbol{u}_{\mathrm{s}}(\boldsymbol{x},t)\cdot\boldsymbol{u}_{\mathrm{s}}(\boldsymbol{x}+\boldsymbol{x}_{\mathrm{L}}+\boldsymbol{x}_{\mathrm{s}},t)\rangle - \langle \boldsymbol{u}_{\mathrm{s}}(\boldsymbol{x},t)\cdot\boldsymbol{u}_{\mathrm{s}}(\boldsymbol{x}+\boldsymbol{x}_{\mathrm{L}},t)\rangle|,$

then from (C 6), we have

$$\Delta R^{\mathrm{L}} \sim (|\boldsymbol{x}_{\mathrm{s}}|^{\frac{2}{3}}\epsilon^{\frac{2}{3}})^{\frac{1}{2}}(\epsilon l_{\mathrm{s}})^{\frac{1}{2}} \sim (\tau^{\frac{1}{2}}\epsilon^{\frac{1}{4}+\frac{1}{3}})^2 \sim \epsilon\tau. \tag{C 8}$$

Therefore, we have

$$R_{11}^{\mathrm{L}}(\tau) = \langle u_{\mathrm{s}}^2\rangle - \pi C^{\mathrm{L}}\epsilon\tau, \tag{C 9}$$

where $C^{\mathrm{L}} \approx C^{\mathrm{EL}}$.

REFERENCES

Anselmet, F., Gagne, Y., Hopfinger, E. J & Antonia, R. A. 1984 Higher-order velocity structure functions in turbulent shear flows. *J. Fluid Mech.* **140**, 63–89.

Batchelor, G. K. 1951 Pressure fluctuations in isotropic turbulence. *Proc. Camb. Phil. Soc.* **47**, 359–374.

BATCHELOR, G. K. 1953 *The Theory of Homogeneous Turbulence*. Cambridge University Press.

BATCHELOR, G. K. 1959 Small-scale variation of convected quantities like temperature in turbulent fluid. Part 1. General discussion and the case of small conductivity. *J. Fluid Mech.* **5**, 113–133.

BATCHELOR, G. K. & TOWNSEND, A. A. 1947 Decay of vorticity in isotropic turbulence. *Proc. R. Soc. Lond.* A **190**, 534–560.

BROADWELL, J. F. & BREIDENTHAL, R. E. 1982 A simple model of mixing and chemical reaction in a turbulent shear layer. *J. Fluid Mech.* **125**, 397–410.

CARRUTHERS, D. J., FUNG, J. C. H., HUNT, J. C. R. & PERKINS, R. J. 1990 The emergence of characteristic (coherent?) motion in homogeneous turbulent shear flows. In *Turbulence and Coherent Structures, Proc. Grenoble Conference 1989* (ed. M. Lesieur & O. Métais) Kluwer.

CARRUTHERS, D. J. & HUNT, J. C. R. 1986 Velocity fluctuations near an interface between a turbulent region and a stably stratified layer. *J. Fluid Mech.* **165**, 475–501.

CHASE, D. M. 1970 Space-time correlations of velocity and pressure and the role of convection for homogeneous turbulence in the universal range. *Acustica* **22**, 303–320.

COMTE-BELLOT, G. & CORRSIN, S. 1971 Simple Eulerian time correlation of full- and narrow-band velocity signals in grid-generated, isotropic turbulence. *J. Fluid Mech.* **48**, 273–337.

DRUMMOND, I. T., DUANE, S. & HORGAN, R. R. 1984 Scalar diffusion in simulated helical turbulence with molecular diffusivity. *J. Fluid Mech.* **138**, 75–91.

DURBIN, P. A. & HUNT, J. C. R. 1980 Dispersion from elevated line sources in turbulent boundary layers. *J. Méc.* **19**, 679–695.

EDWARDS, S. F. 1964 The statistical dynamics of homogeneous turbulence. *J. Fluid Mech.* **18**, 239–273.

FAVRE, A. J., GAVIGLIO, J. J. & DUMAS, R. 1957 Space-time double correlations and spectra in a turbulent boundary layer. *J. Fluid Mech.* **2**, 313–342.

FERMIGIER, M. 1980 Ph.D. dissertation. *L'Universite Pierre Et Marie Curie, Paris.*

FUNG, J. C. H. 1990 Kinematic simulation of turbulent flow and particle motions. Ph.D. dissertation, University of Cambridge.

FUNG, J. C. H, HUNT, J. C. R., PERKINS, R. J., WRAY, A. A. & STRETCH, D. 1991 Defining the zonal structure of turbulence using the pressure and invariants of the deformation tensor. In *Proc. Third European Turbulence Conference, Stockholm, 1990* (ed. A. V. Johansson & P. H. Alfredsson). Springer.

GEORGE, W. K., BEUTHER, P. D. & ARNDT, R. E. A. 1984 Pressure spectra in turbulent free shear flows. *J. Fluid Mech.* **148**, 155–191.

GIBSON, M. M. 1963 Spectra of turbulence in a round jet. *J. Fluid Mech.* **15**, 161–173.

GRANT, H. L., STEWART, R. W. & MOILLIET, A. 1962 Turbulent spectra from a tidal channel. *J. Fluid Mech.* **12**, 241–268.

HANNA, S. R. 1981 Lagrangian and Eulerian time-scale relation in the daytime boundary layer. *J. Appl. Met.* **20**, 242–249.

HINZE, J. O. 1975 *Turbulence*. McGraw-Hill.

HUNT, J. C. R. 1973 A theory of turbulent flow round two-dimensional bluff bodies. *J. Fluid Mech.* **61**, 625–706.

HUNT, J. C. R. 1985 Turbulent diffusion from sources in complex flows. *Ann. Rev. Fluid Mech.* **17**, 447–485.

HUNT, J. C. R., AUTON, T. R., SENE, K., THOMAS, N. M. & KOWE, K. 1988 Bubble motions in large eddies and turbulent flows. In *Proc. Conf. Transient Phenomena in Multiphase Flow* (ed. N. H. Afgan). Hemisphere.

HUNT, J. C. R., BUELL, J. C. & WRAY, A. A. 1987 Big whorls carry little whorls. *NASA Rep.* CTR-S87.

HUNT, J. C. R., FUNG, J. C. H., MALIK, N. A., PERKINS, R. J., VASSILICOS, J. C., WRAY A. A., BUELL, J. . & BERTOGLIO, J. P. 1991 Kinematics of small scale motions in homogeneous isotropic turbulence. In *Proc. Third European Turbulence Conference, Stockholm, 1990* (ed. A. V. Johansson & P. H. Alfredsson). Springer.

INOUE, E. 1951 On turbulent diffusion in the atmosphere. *J. Met. Soc. Japan* **29**, 246–252.

KOLMOGOROV, A. N. 1941 The local structure of turbulence in incompressible viscous fluid for very large Reynolds numbers. *Dokl. Akad. Nauk SSSR* **30**, 301–305.

KOLMOGOROV, A. N. 1962 A refinement of previous hypotheses concerning the local structure of turbulence on a viscous incompressible fluid at high Reynolds number. *J. Fluid Mech.* **13**, 82–85.

KRAICHNAN, R. H. 1966 Dispersion of particles pairs in homogeneous turbulence. *Phys. Fluids* **9**, 1728–1752.

KRAICHNAN, R. H. 1970 Diffusion by a random velocity field. *Phys. Fluids* **13**, 22–31.

LARCHEVÊQUE, M. & LESIEUR, M. 1981 The application of eddy-damped markovian closures to the problem of dispersion of particle pairs. *J. Méc.* **20**, 113–134.

LEE, M. J., KIM, J. & MOIN, P. 1990 Structure of turbulence at high shear rate. *J. Fluid Mech.* **216**, 561–584.

LESLIE, D. C. 1973 *Developments in the Theory of Turbulence*. Clarendon.

LUNDGREN, R. H. 1981 Turbulent pairs dispersion and scalar diffusion. *J. Fluid Mech.* **111**, 27–57.

MALIK, N. A. 1991 Studies in turbulent dispersion using kinematic simulation. Ph.D. dissertation. University of Cambridge.

MAXEY, M. R. 1987 The motion of small spherical particles in a cellular flow field. *Phys. Fluids* **30**, 1915–1928.

MOIN, P. & MOSER, R. D. 1989 Characteristic-eddy decomposition of turbulence in a channel. *J. Fluid Mech.* **200**, 471–510.

MONIN, A. S. & YAGLOM, A. M. 1975 *Statistical Fluid Mechanics*. Vol. 2. MIT Press.

NOVIKOV, E. A. 1963 Random force method in turbulence theory. *Sov. Phys. JETP* **17**, 1449–1453.

OBUKHOV, A. 1941 Spectral energy distribution in a turbulent flow. *Izv. Akad. Nauk. SSSR, Ser. Geogr. i Geofiz.* **5**, 453–466. (Translation: Ministry of Supply, p. 211097).

PERKINS, R. J., CARRUTHERS, D. J., DRAYTON, M. J. & HUNT, J. C. R. 1990 Turbulence and diffusion at density interfaces. In *Phase-Interface Phenomena in Multiphase Flow* (ed. G. F. Hewitt, F. Mayinger & J. R. Riznic), pp. 21–30. Hemisphere.

PERRY, A. E. & CHONG, M. S. 1987 A description of eddying motions and flow patterns using critical-point concepts. *Ann. Rev. Fluid Mech.* **19**, 125–55.

PETERS, N. & WILLIAMS, F. A. 1988 *22nd Symp. on Combustion, Seattle.*

REEKS, M. W. 1977 On the dispersion of small particles suspended in an isotropic turbulent fluid. *J. Fluid Mech.* **83**, 529–546.

RICHARDSON, L. F. 1926 Atmospheric diffusion shown on a distance-neighbour graph. *Proc. R. Soc. Lond.* A **110**, 709–737.

ROGALLO, R. S. & MOIN, P. 1984 Numerical simulation of turbulent flows. *Ann. Rev. Fluid Mech.* **16**, 99–157.

SCHWARZ, K. W. 1990 Evidence for organized small-scale structure in fully developed turbulence. *Phys. Rev. Lett.* **64**, 415–418.

SHLIEN, D. J., & CORRSIN, S. 1974 A measurement of Lagrangian velocity autocorrelations in approximately isotropic turbulence. *J. Fluid Mech.* **62**, 225–271.

SNYDER, W. H. & LUMLEY, J. L. 1971 Some measurements of particle velocity autocorrelation functions in a turbulent flow. *J. Fluid Mech.* **48**, 47–71.

SQUIRES, K. D. 1990 The interaction of particles with homogeneous turbulence. Ph.D. dissertation, University of Stanford.

TATARSKI, V. I. 1960 Radiophysical methods of investigating atmospheric turbulence. *Izv. Vyssh. Uchebn. Zaved. 3 Radiofizika* **4**, 551–583.

TAYLOR, G. I. 1921 Diffusion by continuous movements. *Proc. Lond. Math. Soc.* **20**, 196–211.

TENNEKES, H. 1975 Eulerian and Lagrangian time microscales in isotropic turbulence. *J. Fluid Mech.* **67**, 561–567.

THOMSON, D. J. 1987 Criteria for the selection of stochastic models of particle trajectories in turbulent flows. *J. Fluid Mech.* **180**, 529–556.

THOMSON, D. J. 1990 A stochastic model for the motion of particle pairs in isotropic high

Reynolds number turbulence, and its application to the problem of concentration variance. *J. Fluid Mech.* **210**, 113–153.

TOWNSEND, A. A. 1976 *The Structure of Turbulent Shear Flow.* Cambridge University Press.

TURFUS, C. & HUNT, J. C. R. 1987 A stochastic analysis of the displacements of fluid element in inhomogeneous turbulence using Kraichnan's method of random modes. In *Advances in Turbulence* (ed. G. Comte-Bellot & J. Mathieu), pp. 191–203. Springer.

VAN ATTA, C. W. & CHEN, W. Y. 1970 Structure functions of turbulence in the atmospheric boundary layer over the ocean. *J. Fluid Mech.* **44**, 147–159.

VINCENT, V. & MENEGUZZI, M. 1991 The spatial structure and statistical properties of homogeneous turbulence. *J. Fluid Mech.* **225**, 1–20.

WILKINS, E. M. 1958 Observations on the separation of pairs of neutral balloons and applications to atmospheric diffusion theory. *J. Met.* **17**, 324-327.

WRAY, A. & HUNT, J. C. R. 1990 Algorithms for classification of turbulent structures. In *Proc. IUTAM Symp. on Topological Fluid Mechanics* (ed. H. K. Moffatt & A. Tsinober), pp. 95–104. Cambridge University Press.

YEUNG, P. K. & POPE, S. B. 1989 Lagrangian statistics from direct numerical simulations of isotropic turbulence. *J. Fluid Mech.* **207**, 531–586.